Nuclear Materials and Energy 26 (2021) 100862

Contents lists available at ScienceDirect

Nuclear Materials and Energy

journal homepage: www.elsevier.com/locate/nme

# Determination of electron backscattering coefficient of beryllium by a high-precision Monte Carlo simulation

Abrar Hussain [a,1], Lihao Yang [a,1], Shifeng Mao [b,*], Bo Da [c], Károly Tőkési [d,*], Z.J. Ding [a,*]

[a] Hefei National Laboratory for Physical Sciences at Microscale and Department of Physics, University of Science and Technology of China, Hefei, Anhui 230026, PR China
[b] Department of Engineering and Applied Physics, University of Science and Technology of China, Hefei, Anhui 230026, People's Republic of China
[c] Research and Services Division of Materials Data and Integrated System (MaDIS), National Institute for Materials Science, 1-1 Namiki Tsukuba, Ibaraki 305-0044, Japan
[d] Institute for Nuclear Research, (ATOMKI), Debrecen, Hungary

ARTICLE INFO

*Keywords:*
Monte Carlo simulation
Backscattering
Beryllium
Boron
Carbon
Contamination

ABSTRACT

We present an up-to-date Monte Carlo simulation of electron backscattering coefficient of beryllium, which is an important material in fusion reactor, at an impact energy range of electrons between 100 eV and 100 keV. The Mott's cross section calculated with more accurate scattering potential and a relativistic dielectric functional formalism with full Penn algorithm and experimental optical data are used in the modelling of electron elastic and inelastic scatterings, respectively. This Monte Carlo simulation modelling enabled us to derive comprehensive theoretical values of backscattering coefficient, which are found significantly smaller than the previous published experimental data particularly at energies below 10 keV. Simulation of electron backscattering spectra was then carried out with and without Auger electron emission, which confirmed that Auger electrons have negligible contribution to backscattering coefficient. To validate our simulation results, we have also performed calculation for amorphous boron and carbon, while the comparison with the available experimental data shows reasonable agreement. Further simulation for carbon and water covered Be sample has revealed that the surface contamination in low vacuum conditions with several atomic/molecular layers can drastically alter the measurement values for beryllium at low energies. The low backscattering coefficient values of beryllium are partly attributed to the extremely strong forward elastic scattering for low atomic number element. Therefore, we recommend to use the here reported backscattering coefficient data of beryllium for applications.

## 1. Introduction

Beryllium is selected as the first wall material in ITER [1] due to the following advantages. As a low Z material, it can be compatible with high performance core plasma without significant fuel dilution and radiation. It is non-reactive with hydrogen isotopes to avoid the tritium retention issue. Furthermore, it has good thermal conductivity and oxygen gettering ability [2]. Although beryllium has important application in the fusion reactor, there are very limited and old data available for studies of its interactions with charged particles, especially electrons, in the incident energy range of 0.1–100 keV. Only a few investigations exist for the determination of the electron backscattering coefficient [3]. The backscattering coefficient is a quantity to characterize the amount of backscattered electrons by bombarding a solid surface with an incident electron beam. When primary electrons penetrate a material they undergo elastic and inelastic collisions during their motion in matter before either losing all energies in the bulk or emitting from sample surface. During the inelastic collision processes secondary electrons can be generated. Empirically one separates the emitted electrons according to their kinetic energies and defines them as secondary electrons if their energies are below 50 eV and as backscattered electrons otherwise. Denoting the backscattering coefficient by $\eta$ (the number of backscattered electrons of energies greater than 50 eV per an incident electron) and the secondary electrons yield by δ, the total electron yield is hence the sum of them.

During the last decades many experiments have been performed to explore the general tendency of dependence of backscattering coefficient on atomic number of the target and incident electron energy. It was observed that the backscattering coefficient increases with atomic

* Corresponding authors.
*E-mail addresses:* sfmao@ustc.edu.cn (S. Mao), tokesi@atomki.hu (K. Tőkési), zjding@ustc.edu.cn (Z.J. Ding).
[1] A. Hussain and L.H. Yang contributed equally to the work.

https://doi.org/10.1016/j.nme.2020.100862
Received 3 June 2020; Received in revised form 21 November 2020; Accepted 25 November 2020
Available online 8 December 2020

number at high energies above 10 keV [4–6]. The general behaviour of the primary energy dependence of backscattering coefficient was also found as [7–9]: a) for low atomic number solids ($Z < 20$) it decreases with increasing of incident energy; b) for high-$Z$ elements ($Z > 26$) it increases with incident energy; c) it is almost constant for intermediate value $Z$-elements [10]. It was also observed that, at low primary energies $\eta$ is surface sensitive [11]. Joy has compiled these historical measurement data into a database for many elemental solids and compounds without including uncertainty and judging the reliability [12].

For Be sample, Martin et al. had performed experimental investigations of the energy and angular distribution of backscattered electrons at high energies, in the incident energy range between 43.5 keV and 124 keV [13]. Reimer and Tollkamp had measured $\eta$ as a function of primary energy for a normal incident beam in a scanning electron microscope. They have found that $\eta$ increases with decreasing primary energy particularly below 5 keV [14]. Bronshtein and Fraiman had performed backscattering coefficient measurements up to 4 keV primary energy [15]. Shimizu had measured the backscattering coefficients with a spherical symmetric electron energy analyser in an ultrahigh vacuum (UHV) system, and compared experimental data with his Monte Carlo calculations [16]. These measurement data are scattered in a rather large range, from 57% difference at 1 keV down to 40% at ~ 10 keV. The only available theoretical data were provided by Shimizu who used a Monte Carlo simulation technique to calculate backscattering coefficient as a function of the incident electron energy above 5 keV [16]. He used the stopping power formula of Spencer and Fano [17] in the continuous slowing down approximation for the calculation of electron energy loss and Rutherford scattering formula for describing electron elastic cross section [16], but the approximations of this theoretical framework are now known to be poor, particularly at low electron energies [6,18].

Monte Carlo method is a powerful theoretical tool widely used for study of particle interaction with matter [18–20]. In recent decades we have continuously improved Monte Carlo modeling of electron beam interaction with solids and surfaces by employing modern knowledge and theories of electron scattering in matter. The systematically developed Monte Carlo simulation models and methods by Ding's group (DingMC) in different approaches for applications to electron spectroscopies and electron microscopies are comprised of two categories: 1. Classical trajectory Monte Carlo (CTMC) simulations, where the simulation of electron elastic and inelastic scattering in amorphous-like surfaces/solids/thin-films are treated by conventional Monte Carlo sampling techniques from respective scattering cross sections, including (a) CTMC-SEM, simulation of secondary electrons and backscattered electrons emitted from bulk solids as signals in scanning electron microscopy and background in Auger electron spectroscopy [21–38]; (b) CTMC-3DSEM, simulation for complex 3D sample geometries particularly for critical dimension scanning electron microscopic imaging [39–49]; [c] CTMC-EPMA, simulation of continuous and characteristic X-ray signals in electron probe microanalysis [50–52]; (d) CTMC-SES, simulation of Auger electron and/or X-ray photoelectron signals in surface electron spectroscopies [53–56]; (e) CTMC-REELS, simulation of electron elastic peak spectroscopy and reflection electron energy loss spectroscopic spectrum from surfaces [57–66]; (f) CTMC-RMC, a reverse Monte Carlo method for deriving optical constants of solids from reflection electron energy loss spectroscopy spectra [67–73]; (g) CTMC-CHARG, simulation of specimen charging phenomena in insulators and semiconductors [74–78]; (h) CTMC-ATOMIC, simulation for atomic thin layers with substrate [63,66] or without substrate, like graphene, particularly for deriving electron inelastic scattering mean free path [79–81]; 2. Quantum trajectory Monte Carlo (QTMC) simulation for crystalline materials, which combines the simulation of Bohmian quantum trajectories for electron elastic scattering/diffraction [82–84] with the Monte Carlo sampling of electron inelastic scattering: QTMC-ARSEI, for atomic resolution secondary electron imaging in scanning transmission electron microscopy [85–87].

In this work we employ an up-to-date simulation model of CTMC-SEM to study electron backscattering coefficient. This model configuration uses the best available scattering potential for the calculation of relativistic elastic scattering cross section; in addition, the relativistic form of dielectric functional formulation of electron inelastic scattering cross section in full Penn algorithm is adopted. The backscattering energy spectrum and backscattering coefficient from beryllium sample are investigated theoretically at electron impact energies between 0.1 and 100 keV with and without the Auger electron emission taken into account. Our simulations consider both the individual elastic and inelastic scattering of primary electrons and include the high energy cascade secondary electron production during electron transport inside the bulk beryllium. The primary purpose of this work was to try to reduce the uncertainty range of the experimental data distribution by a high accuracy Monte Carlo simulation, and especially predict the reasonable values at low primary energies below 1 keV where the experimental data are rare. However, the simulation has led to a new finding of extremely low backscattering coefficient values, particularly below 10 keV, as compared with the previous experimental data and also with that of the closest elemental solids, boron and carbon. While the comparisons with experiments in cases of boron and carbon are very reasonable, there is a quite large difference between the present calculation and experimental data. The present calculation predicts backscattering coefficient values by the lower limit of experimental data range at very high primary energies, and even becomes much smaller than experimental data with decreasing primary energy. By considering the surface contamination very likely to be presented in early experiments the difference between experimental observation and theoretical calculation can be explained. The reason for such very low backscattering coefficient values for beryllium has been analysed to be attributed to the especially strong forward elastic scattering of beryllium atoms, and electron scattering mean free paths.

## 2. Monte Carlo model

In our simulation both the elastic and inelastic scatterings of primary electrons and also the secondary electron production during transport of the electrons inside beryllium are taken into account. Details of the calculation procedure are described elsewhere [27,32], here the outline of our calculation procedure is briefly introduced while we mainly emphasis on the new feature of this up-to-date CTMC-SEM model.

Elastic cross section

For the elastic scattering of electrons, we used the Mott's differential cross section [88],

$$\frac{d\sigma_e}{d\Omega} = |f(\theta)|^2 + |g(\theta)|^2 \tag{1}$$

where $f(\theta)$ and $g(\theta)$ are the scattering amplitudes and can be calculated with the partial wave expansion method by solving Dirac equation,

$$f(\theta) = \frac{1}{2ik}\sum_{l=0}^{\infty}\left\{(l+1)\left(e^{2i\delta_\ell^+} - 1\right) + l\left(e^{2i\delta_\ell^-} - 1\right)\right\}P_\ell(cos\theta) \tag{2}$$

$$g(\theta) = \frac{1}{2ik}\sum_{\ell=1}^{\infty}\left\{-e^{2i\delta_\ell^+} + e^{2i\delta_\ell^-}\right\}P_\ell^1(cos\theta) \tag{3}$$

where $\delta_l^+$ and $\delta_l^-$ are spin up and spin down phase shifts of the $\ell$th partial wave, respectively; $P_\ell(cos\theta)$ and $P_\ell^1(cos\theta)$ are the Legendre and the first order associated Legendre functions, respectively.

The scattering potential used in the present model is expressed as,

$$V(r) = V_{st}(r) + V_{ex}(r) + V_{cp}(r) \tag{4}$$

where $V_{st}$ is the electrostatic potential, $V_{ex}$ is the electron exchange potential and $V_{cp}$ is the correlation-polarization potential. The electrostatic potential for the interaction between an electron and the target atom is

$$V_{st}(r) = -e[\varphi_n(r) + \varphi_e(r)] \tag{5}$$

where $\varphi_n$ and $\varphi_e$ are respectively the components of nucleus and the

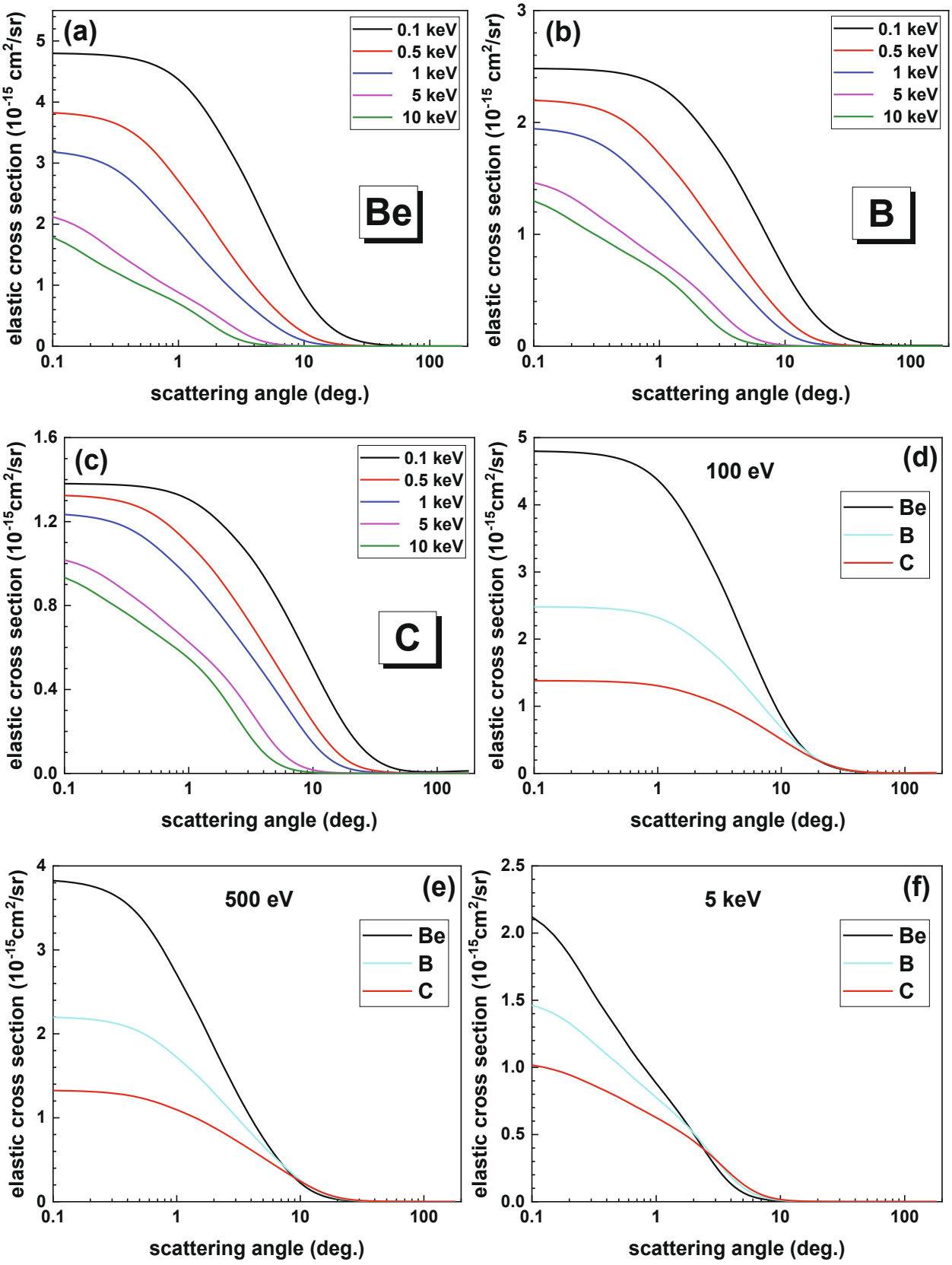


**Fig. 1.** Electron differential elastic scattering cross section as a function of scattering angle at different energies for: (a) beryllium, (b) boron and (c) carbon. Comparison for all the three elements at the energies of: (d) 0.1 keV, (e) at 0.5 keV and (f) 5 keV.

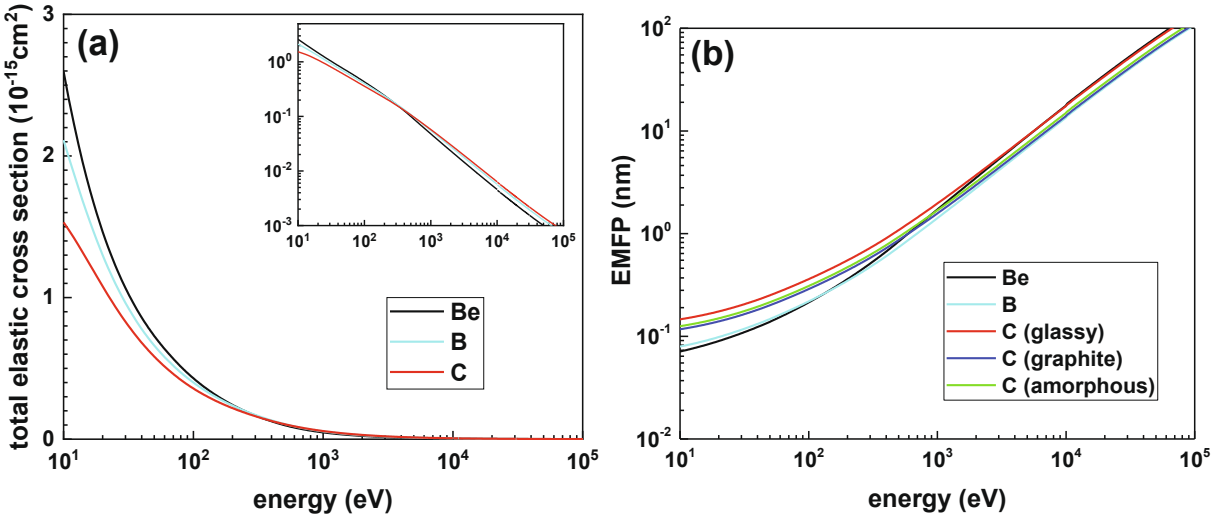


**Fig. 2.** (a) Total elastic scattering cross section and (b) elastic mean free path as functions of energy for five materials, beryllium, boron and carbon allotropes (glassy, amorphous and graphite).

electron cloud of electrostatic potential,

$$\varphi_n(r) = e\left(\frac{1}{r}\int_0^r \rho_n(r')4\pi r'^2 dr' + \int_r^\infty \rho_n(r')4\pi r' dr'\right) \tag{6}$$

$$\varphi_e(r) = -e\left(\frac{1}{r}\int_0^r \rho_e(r')4\pi r'^2 dr' + \int_r^\infty \rho_e(r')4\pi r' dr'\right) \tag{7}$$

where $\rho_n$ is the nuclear charge distribution and $\rho_e$ is the electron charge distribution of the target atom. A Fermi distribution is used for the determination of the nuclear charge distribution [89],

$$\rho_{n,F}(r) = \frac{\rho_0}{exp[(r-R_n)/z]+1} \tag{8}$$

where $R_n = 1.07\times10^{-13}A^{1/3}$ (cm) and $z = 5.46\times10^{-14}$ (cm), $A$ is the atomic mass (amu) of the element. The constant $\rho_0$, which is twice the proton density at $r = R_n$, is to be determined by normalization. The most accurate electron densities available for free atoms are obtained from self-consistent relativistic Dirac-Fock (DF) calculations. The numerical DF densities calculated by the multiconfiguration DF program of Desclaux [90] are used here for determination of the electron charge distribution.

The Furness-McCarthy exchange potential [91] is used for the electron exchange potential:

$$V_{ex,FM}(r) = \frac{1}{2}[E - V_{st}(r)] - \frac{1}{2}\{[E - V_{st}(r)]^2 + 4\pi a_0 e^4 \rho_e(r)\}^{1/2} \tag{9}$$

When the projectile is far from the atom, the polarization potential energy can be approximated by means of the Buckingham potential,

$$V_{cp,B}(r) = -\frac{\alpha_d e^2}{2\left(r^2+d^2\right)^2} \tag{10}$$

where $\alpha_d$ is dipole polarizability of the target atom and $d$ is a phenomenological cut-off parameter that serves to prevent the polarization potential from diverging at $r = 0$. The experimental values of the atomic dipole polarizabilities from Ref. [92] are usually used in Eq. (10). Mittleman and Watson [93] proposed an expression for the cut-off parameter, $d^4 = \frac{1}{2}\alpha_d a_0 Z^{-1/3} b_{pol}^2$, where $Z$ is the atomic number and $b_{pol}$ is an adjustable energy-dependent parameter, $b_{pol}^2 = max\{(E-50\text{ eV})/(16\text{ eV}), 1\}$. Perdew and Zunger [94] proposed a parameterization of the correlation potential:

$$V_{cp}(r) = \begin{cases} -\dfrac{e^2}{a_0}(0.0311 ln r_s - 0.0584 + 0.00133 r_s ln r_s - 0.0084 r_s), & r_s < 1; \\ -\dfrac{e^2}{a_0}\dfrac{0.1423 + 0.1748 r_s^{1/2} + 0.0633 r_s}{\left(1 + 1.0529 r_s^{1/2} + 0.3334 r_s\right)^2}, & r_s \geqslant 1. \end{cases} \tag{11}$$

where

$$r_s = \frac{1}{a_0}\left[\frac{3}{4\pi\rho_e(r)}\right]^{1/3} \tag{12}$$

is the radius of the sphere that contains (on average) one electron of the gas, in units of the Bohr radius $a_0$. A more accurate correlation-polarization potential combines the long-range polarization potential (Eq. (10)) with the correlation potential $V_{cp}(r)$ obtained from the local-density approximation (LDA) which is expressed as [95],

$$V_{cp,LDA}(r) \equiv \begin{cases} max\{V_{co}(r), V_{cp,B}(r)\}, & r < r_{cp}; \\ V_{cp,B}(r), & r \geqslant r_{cp}. \end{cases} \tag{13}$$

where $r_{cp}$ is the outer radius at which $V_{cp}(r)$ and $V_{cp,B}(r)$ cross. All the calculation of elastic cross section are performed by the Fortran 77 code, ELSEPA [96].

Fig. 1 shows the primary electron energy and scattering angle dependent elastic cross sections of Be. Generally, with increasing incident energy the elastic cross sections are decreasing. The highest elastic cross sections are in forwards angles. Then the elastic cross sections decrease rapidly with the increasing scattering angle. We note that at low primary energies, the elastic cross sections increase above $90^0$, showing the importance of the electron backscattering at low impact energies.

Fig. 1(d) also shows the variation of electron elastic cross section with scattering angles and material nature. It is observed that elastic cross section for lower atomic number element Be is higher than the higher atomic number elements, B and C. These variations strongly affect the results of backscattering coefficients.

The integration of the differential cross section over total solid angles gives us the total elastic cross sections as,

$$\sigma_e = \int \frac{d\sigma_e}{d\Omega}\, d\Omega = 2\pi \int_0^\pi sin\theta\{|f(\theta)|^2 + |g(\theta)|^2\}\, d\theta \tag{14}$$

Fig. 2(a) shows the total elastic cross sections as a function of energy for the simulated materials i.e. Be, B and C. The total elastic cross section

**Table 1**
Mass density $\rho$ and atom number density $n_a$ for five elemental materials, i.e. beryllium, boron and carbon allotropes (glassy, amorphous and graphite), where $N_A$ is Avogadro constant and $M$ is atomic weight.

| elements | $\rho$(g/cm$^3$) | $n_a = N_A\rho/M$(10$^{23}$ atoms/cm$^3$) |
|---|---|---|
| Be | 1.85 | 1.236 |
| B | 2.34 | 1.3034 |
| C (glassy) | 1.80 | 0.9024 |
| C (amorphous) | 2.10 | 1.0528 |
| C (graphite) | 2.25 | 1.1280 |

for the energy lower than almost 250 eV is found lower for the heavier element C, however, at the higher energy, this variation becomes reverse. In order to compare with electron inelastic mean free path (IMFP) $\lambda_{in}$, we also plot in Fig. 2(b) the electron elastic mean free path, $\lambda_e = 1/n_a\sigma_e$, where $n_a$ is atom number density given in Table. 1, for five materials, i.e. beryllium, boron and carbon allotropes (glassy, amorphous and graphite), considered in simulation.

Inelastic cross section

For the description of the electron inelastic scattering processes, we used the dielectric function formalism with which the specific electronic excitations a particular sample can be considered. In this model, the differential inverse inelastic mean free path (DIIMFP) for moving electrons in a material is given as:

$$\frac{d^2\lambda_{in}^{-1}}{d(\hbar\omega)dq} = \frac{2\gamma^2}{1+\gamma}\frac{1}{\pi a_0 E}\mathrm{Im}\left\{\frac{-1}{\varepsilon(q,\omega)}\right\}\frac{1}{q} \tag{15}$$

where $\gamma = 1 + E/(m_0c^2)$ is the relativistic correction factor, $m_0$ the mass of electron, $m_0c^2$ the static energy of an electron. The coefficient, $2\gamma^2/(1+\gamma)$, in Eq. (15) is due to the relativistic effect; $\varepsilon(q,\omega)$ is the complex dielectric function of medium as a function of energy loss $\hbar\omega$ and momentum transfer $\hbar q$ for characterizing the electronic excitation; $a_0$ is Bohr's radius and $\lambda_{in}$ is the electron inelastic mean free path (IMFP). The term $Im\{-1/\varepsilon(q,\omega)\}$ is known as the energy loss function (ELF) which determines the probability of inelastic scattering events. Penn had suggested an algorithm, the full Penn algorithm (FPA), for the extension of the electron energy loss function from the optical limit of $q \to 0$, $Im\{-1/\varepsilon(q=0,\omega)\}$, into the $(q,\omega)$-plane, $Im\{-1/\varepsilon(q,\omega)\}$ [97]. Using the Lindhard dielectric function $\varepsilon_L(q,\omega;\omega_p)$, the ELF can be written as:

$$\mathrm{Im}\left\{\frac{-1}{\varepsilon(q,\omega)}\right\} = \int_0^\infty g(\omega_p)\mathrm{Im}\left\{\frac{-1}{\varepsilon_L(q,\omega;\omega_p)}\right\}d\omega_p \tag{16}$$

where $g(\omega)$ is the expansion coefficient, and it is related to the optical ELF, $\mathrm{Im}\{-1/\varepsilon(0,\omega)\}$, according to the following equation:

$$g(\omega) = \frac{2}{\pi\omega}\mathrm{Im}\left\{\frac{-1}{\varepsilon(0,\omega)}\right\} \tag{17}$$

It was shown that this approach yields closer simulation results to the experimental data, either backscattering coefficient or the energy distribution of electrons, than the single-pole approximation (SPA) [32] by which $\mathrm{Im}\{-1/\varepsilon_L(q,\omega;\omega_p)\}$ is simplified as a Dirac $\delta$-function along the plasmon dispersion line [23].

From Eq. (16) the energy loss distribution and IMFP can be obtained respectively by performing the integrations:

$$\frac{d\lambda_{in}^{-1}}{d(\hbar\omega)} = \int_{q_-}^{q_+} dq\frac{d^2\lambda_{in}^{-1}}{d(\hbar\omega)dq} \tag{18}$$

$$\lambda_{in}^{-1} = \int_0^{E-E_F}\frac{d\lambda_{in}^{-1}}{d\omega}\,d\omega \tag{19}$$

where the integration limits, $\hbar q_\pm = \sqrt{m_0E(2 + E/(m_0c^2))} \pm \sqrt{m_0(E-\hbar\omega)(2 + (E-\hbar\omega)/(m_0c^2))}$, are obtained from the energy and momentum conservations. Tanuma et al. have performed extensive calculation of IMFP for nonrelativistic electrons [98–101] and relativistic electrons [102–104]. Recently a machine learning technique is employed for predicting the IMFP and improving empirical formulation [105].

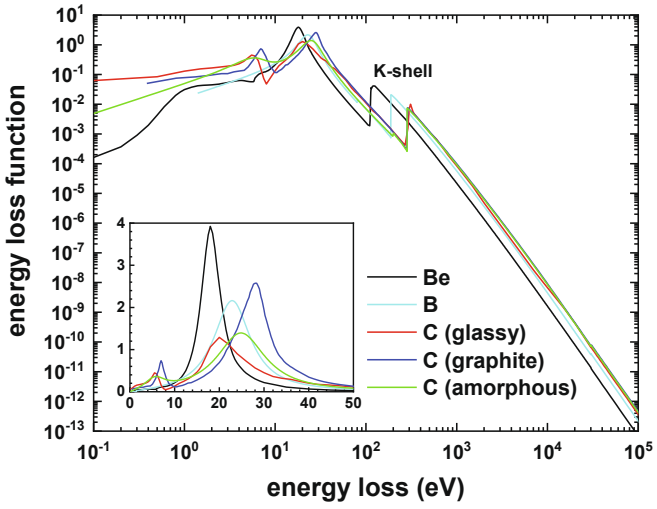


**Fig. 3.** Energy loss functions, $\mathrm{Im}\{-1/\varepsilon(0,\omega)\}$, of beryllium, boron and carbon allotropes (glassy, amorphous and graphite) used in our simulation. The experimental data of dielectric function, $\varepsilon(0,\omega)$, were taken from Palik [106] in the range of 0.02–300 eV and from Henke et al. [107] in the range of 0.3–30 keV for Be, from Prieto et al. [108] in the range of 0–80 eV and from Henke et al. [107] in the range of 0.08–30 keV for B, from Abril et al. [109] in the range of 0–200 eV and from Henke et al. [107] in the range of 0.2–30 keV for amorphous C, from Venghaus [110] in the range of 0.02–40 eV and from Henke et al. [107] in the range of 0.05–30 keV for graphite C, from Hagemann [111] in the range of 0.0001–30 keV for glassy C and atomic scattering factor was used in 30 keV-100 keV [112] for all the simulated materials.

According to the ELF as shown by Fig. 3, the dominant contribution of the energy loss originates from the electronic excitation around several tens eV, and particularly all these elemental materials (Be, B and C) demonstrates a strong plasmon peak around 18–28 eV. For carbon the peak position and intensity varies with the crystalline form: the peak position of $(\pi+\sigma)$ plasmon is 20 eV for glassy carbon, 24.8 eV for amorphous carbon and 28.3 eV for graphite. In addition, there is a weak $\pi$ plasmon around 5.4–6.9 eV for carbon. Fig. 3 also shows the sharp $K$-shell ionization edges around hundred eV, which will play a significant role when the Auger process is taken into account during the simulation.

To check the accuracy of the ELFs used, we applied two well-known sum rules, the perfect screening sum rule (*ps*-sum rule) and the oscillator strength sum rule (*f*-sum rule) [113]. The *f*-sum rule $Z_{eff}$ is given by,

$$Z_{eff} = \frac{2}{\pi\Omega_P^2}\int_0^{\omega_{max}}\omega Im\left\{\frac{-1}{\varepsilon(\omega)}\right\}d\omega \tag{20}$$

where $\hbar\Omega_P = \sqrt{4\pi n_a e^2/m}$. For a very large value of $\omega_{max}$, expectation value of $Z_{eff}$ must be atomic number $Z$, the total number of electrons per atom or molecule.

The *ps*-sum rule $P_{eff}$ can be obtained from the Kramers-Kronig relation as [114,115]:

$$P_{eff} = \frac{2}{\pi}\int_0^{\omega_{max}}\frac{1}{\omega}Im\left\{\frac{-1}{\varepsilon(\omega)}\right\}d\omega + Re\left\{\frac{1}{\varepsilon(0)}\right\} \tag{21}$$

where $Re\{1/\varepsilon(0)\} = 0$ for conductors. The expectation value of $P_{eff}$ is unity in the limit of $\omega_{max}\to\infty$.

Fig. 4 shows the calculated results of *f*-sum rule and *ps*-sum rule for beryllium ($Z = 4$), boron ($Z = 5$) and carbon allotropes ($Z = 6$). For Be the corresponding limit values are $Z_{eff} = 3.96$ and $P_{eff} = 1.05$,

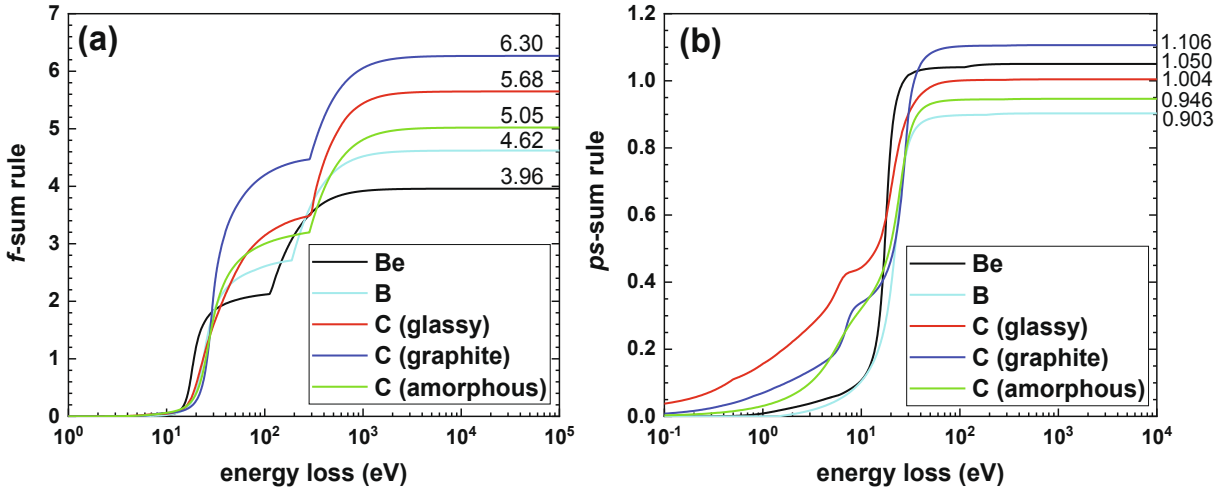


**Fig. 4.** Validation of sum rules for beryllium, boron and carbon allotropes (glassy, graphite and amorphous) as functions of energy loss: (a) *f*-sum rule; (b) *ps*-sum rule.

**Table 2**
Relative errors of sum rules for five elemental materials, i.e. beryllium, boron and carbon allotropes (glassy, amorphous and graphite).

| elements | $Z_{eff}$(%) | $P_{eff}$(%) |
|---|---|---|
| Be | 1.3 | 5.0 |
| B | −8.0 | −10.0 |
| C (glassy) | −5.3 | 0.4 |
| C (amorphous) | −16.0 | −5.4 |
| C (graphite) | 5.0 | 11.0 |

respectively, which are quite close to the nominal values of 4 and 1. Accordingly, the relative errors of sum rules for Be are 1.3% and 5%, respectively. In the previous work of Shinotsuka and Tanuma et. al [102] these errors for $Z_{eff}$ and $P_{eff}$ are 2.4% and 6.6% for Be, respectively. We can conclude that our ELF has enough accuracy for accurate Monte Carlo simulation for Be. While for boron and carbon, there are larger deviations from expectation values, which are listed in Table 2.

Fig. 5(a) shows the comparison on the calculated IMPFs between Be, B and C. For Be, our calculated IMPF agrees very well with Shinotsuka et al. [102] in the energy range of 1–$10^4$ eV. The graphite demonstrates smaller IMFP values, i.e. stronger electron inelastic scattering probability, above 100 eV as compared with glassy and amorphous carbon. This is due to the higher intensity and larger energy values of plasmon peaks of graphite as shown by Fig. 3, while the sum rules indicate that the intensity of ELF is overestimated for graphite.

The electron stopping power is the energy loss travelled per unit distance due to inelastic scattering, $S = -dE/dx$, which was widely used in the early Monte Carlo simulations in the continuous slowing-down approximation. The universal Bethe stopping power equation is written as [116,117],

$$S = 785\frac{Z\rho}{AE}ln\left(\frac{1.166E}{J}\right)\ (\text{in eV/Å}) \tag{22}$$

where $J$ is the mean ionization energy of the target atoms (in eV) and is given by [118,119],

$$J = \begin{cases} 11.5Z, & Z\leqslant 12; \\ 9.76Z + 58.5Z^{-0.19}, & Z\geqslant 13. \end{cases} \tag{23}$$

However, this stopping power presents nonphysical negative values at low energies; several extending formulations have been proposed [120–122]. On the other hand, the electron stopping power can be derived from the dielectric theory [23,123]:

$$S = \int_0^{E-E_F} \omega \frac{d\lambda_{in}^{-1}}{d\omega}\, d\omega \tag{24}$$

Fig. 6 shows the comparison of stopping powers for Be and C allotropes between the present data and the results from other sources [12,116,117,120–123]. In this comparison, the mean excitation energy of Be and graphite is set respectively as 60 and 80 eV [119]. For both Be and carbon cases our results agree well with Shinotsuka's results [123]. Particularly, the present stopping powers of graphite agree well with the experimental data [12], while other theoretical or empirical expressions

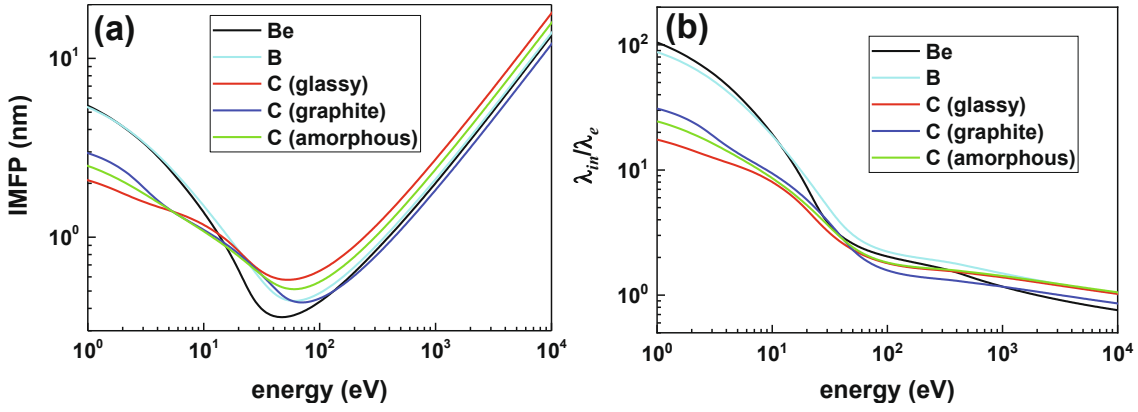


**Fig. 5.** (a) Electron inelastic mean free path and (b) the ratio of electron inelastic mean free to elastic mean free path, as functions of electron energy for all the simulated materials.

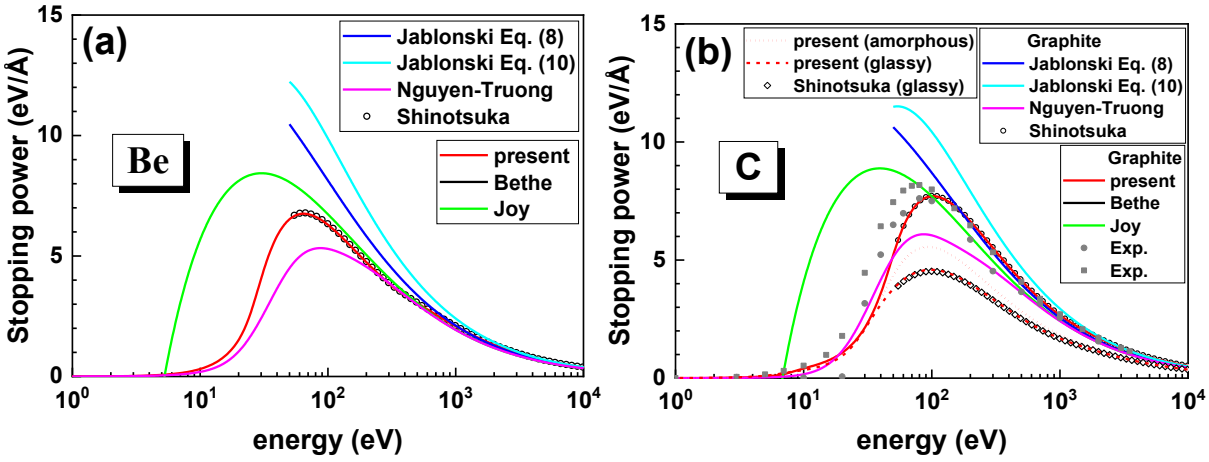


**Fig. 6.** Comparison of stopping powers between the present data and (a) other theoretical results [116,117,120–123] for beryllium, (b) other theoretical/experimental results for carbon [12,116,117,120–123].

show certain differences.

The simulations of the backscattered electron spectra were carried out with and without the Auger electron emission [55,56] taken into account. If the energy loss is less than the binding energy of the corresponding inner-shell (i.e. *K*-shell for Be), $\hbar\omega < E_B$ (where $E_B$ is the binding energy of the inner-shell presented in the optical ELF), then a secondary electron is assumed to be excited from the Fermi sea by transferring $\hbar\omega$ energy from the primary electron to a valence electron of energy with the excitation probability being proportional to a joint density of states of free electrons $\sqrt{E_0(E_0+E_F)}$. If $\hbar\omega > E_B$, the secondary is excited from the inner-shell and has kinetic energy of $\hbar\omega - E_B$. Detailed description of the calculations can be found in Refs. [28,32]. In addition, the relaxation of the excited atom may proceed via two paths: the emission of an Auger electron or the emission of a photon. The sum of the corresponding Auger transition probability, $P_A$, and the corresponding fluorescence transition probability, $P_X$, must be 1. The Auger transition probability, i.e. Auger channel parameter $P_A^X$, for any Auger channel from level $X$, is given by [124],

$$P_A^X = 1 - Z^4/\left(Z^4 + Z_0^4\right) \tag{25}$$

where $Z$ is the atomic number of an element, and $Z_0 = 32.4, 89.4, 155.9$ and 300 for $X = K, L, M$ and $N$, respectively. If $\hbar\omega > E_B$, Auger electron with the energy of 98 eV for Be will be excited with a certain probability ($P_A^{X=K}$).

After undergoing multiple elastic and inelastic scattering collisions inside the sample some electrons will reach back to the surface and only part of them can escape if the following condition is satisfied:

$$E\cos^2\beta > U_0 \tag{26}$$

where $\beta$ is the angle between the electron moving direction and the surface normal, the inner-potential, $U_0$, is the sum of work function and Fermi energy. This condition arises from the fact that the target-vacuum interface has an energy barrier to be overcome by the escaping electron. The electron emission probability from the surface of the material is given by the quantum mechanical transmission function as [18],

$$T(E,\beta) = \begin{cases} \dfrac{4\sqrt{1 - U_0/E\cos^2\beta}}{\left[1 + \sqrt{1 - U_0/E\cos^2\beta}\right]^2}, & \text{if } E\cos^2\beta > U_0; \\ 0, & \text{otherwise.} \end{cases} \tag{27}$$

## 3. Results and discussion

We have performed first the Monte Carlo simulation of the energy spectra of backscattered electrons for mono-energetic primary beam incident on an ideally flat Be surface. For each primary energy we used 1x10$^8$ primary

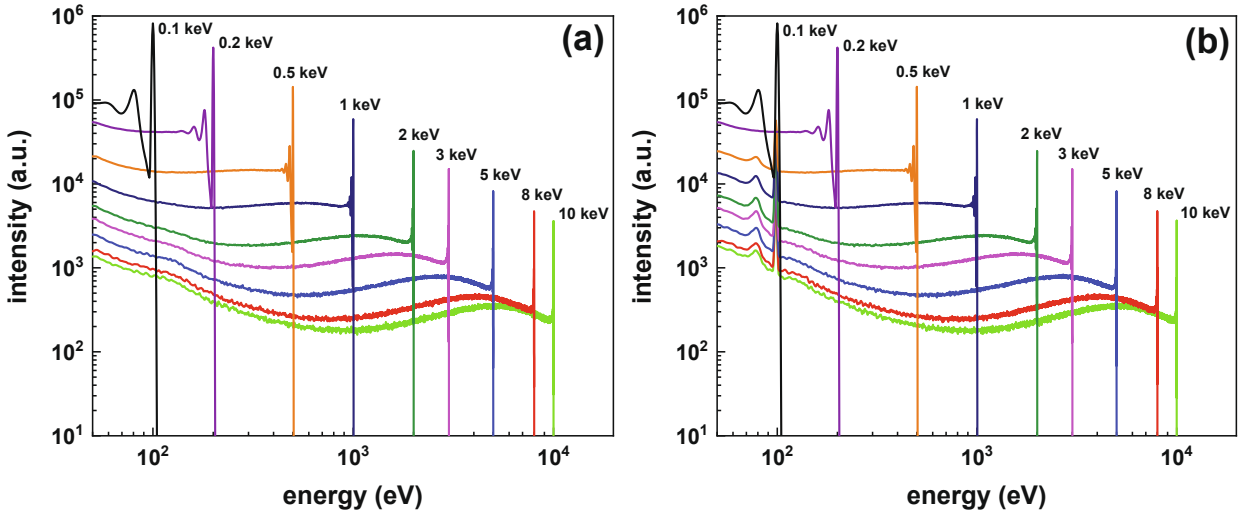


**Fig. 7.** Backscattered electron energy spectra of beryllium for different primary energies and at normal incidence condition: a) without Auger process; b) with Auger process taken into account.

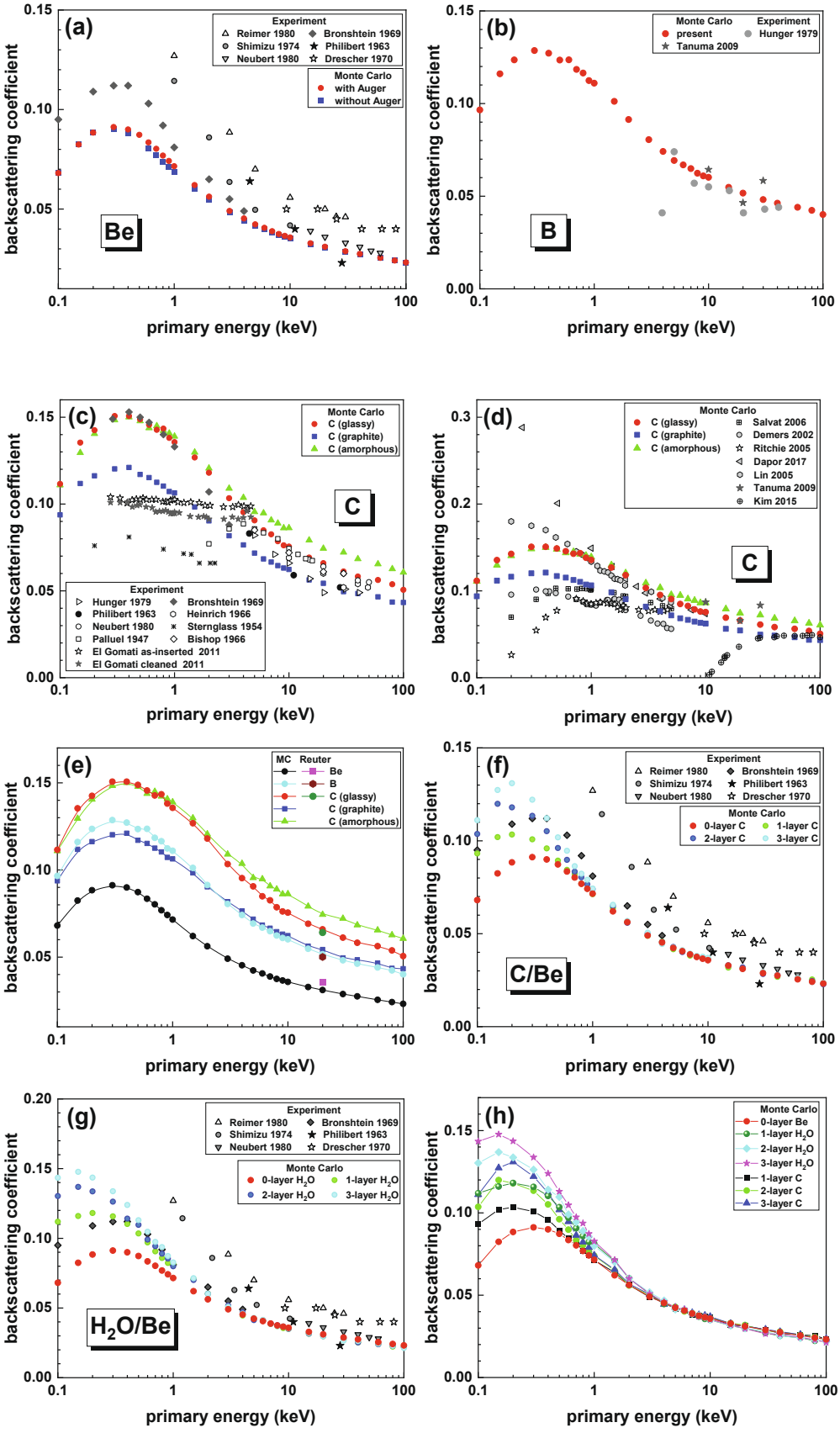


**Fig. 8.** Comparison on the electron backscattering coefficients as functions of primary energy for (a) beryllium, (b) boron and (c) carbon (in different forms), between the present Monte Carlo simulation and experimental data. (d) A comparison on the Monte Carlo simulated backscattering coefficients for carbon between the present simulation and other calculation results. (e) A comparison on the present Monte Carlo simulation for all of the simulated materials, and with Reuter's formula for 20 keV. (f) A comparison on electron backscattering coefficients between the experimental data of beryllium and Monte Carlo simulation for carbon contaminated beryllium surface, which is covered by amorphous carbon at different numbers of atomic layers. (g) A comparison on electron backscattering coefficients between the experimental data of beryllium and Monte Carlo simulation for water adsorbed on beryllium surface, which is covered by amorphous water at different numbers of atomic layers. (h) A comparison on the Monte Carlo simulated backscattering coefficients between the absorbed amorphous carbon and water layers on Be surface.

electron trajectories during a simulation. Fig. 7 shows the simulated backscattered electron energy spectra of beryllium at the incident angle of $0^0$ with respect to the surface normal for several incident electron energies. The simulations were carried out without and with the Auger electron emission taken into account in Fig. 7(a) and 7(b), respectively. In order to smooth the simulated spectra and present finite width of the elastic peak, the convolution has been performed by using a Gaussian function with the standard deviation of 1 eV. We can see clearly the enhanced contributions in the spectra due to the Auger peak around 100 eV compared to the peakless structure in the spectra when the Auger process was neglected. Below the elastic peak there are multiple plasmon peaks corresponding to the plasmon peak of 18 eV observed in ELF of Be (Fig. 3). The log–log plot indicates the tendency of intensity variation with the primary energy. The highest elastically backscattered electron intensity is observed for the lowest incident electron energy. The backscattering coefficient is the area of the spectra; with increasing primary energy the spectra intensity reduces while the energy region expands, so backscattering coefficient may not monotonically change with primary energy.

Counting number of electrons in Fig. 7 according to their emission energy and dividing by the number of incident electrons, we can obtain the backscattering coefficient $\eta$. Fig. 8(a)-8(c) shows the comparison on the primary energy dependence of backscattering coefficients, $\eta(E_p)$, of elemental solids, Be, B and C, with the available experimental data. It can be seen that $\eta$ first increases relatively rapidly with primary energy and then decreases slowly. The maximum $\eta$ is found around 330 eV. The present results in Fig. 7 are displayed in an extended energy range for the linear relationship of $\eta(E_p)\sim lnE_p$ as given in Ref. [125].

In theoretical point of view, the present simulation, combined the best available Monte Carlo technique with the best available ELF, is expected to result in the much more accurate backscattering coefficients than previous theoretical data. From central limit theorem it was expected that the Monte Carlo simulation would produce the theoretical data falling within the range of experimental data distribution, as in the case of previous study for Cu [30]. But quite surprisingly we have found that, in Fig. 8(a), the simulation yields the backscattering coefficient values for Be much smaller than the previously reported experimental data, particularly than the Bronshtein's data [15] at low primary energies below 1 keV, and reach the lower limit of experimental data distribution range above 10 keV [14–16,126–128].

To explore the reason for this difference between the simulation and experiment, we first take the Auger process into consideration in the simulation. However, as indicated by Fig. 8(a) that the contribution of Auger process to backscattering coefficient is negligible. Then we have performed calculations also for the elemental materials having the nearest atomic numbers, i.e. boron and carbon, to validate our Monte Carlo simulation.

For the close atomic number elements, boron and carbon are believed to have quite the similar $\eta(E_p)$ curve shape as well as the close values as beryllium. Fig. 8(b) compare the present calculated results with the available experimental [8] and simulated [129] results for B. Our simulation agrees very well with those data above 5 keV. Fig. 8(c) shows the comparison between present calculated results with the available experimental data [8,15,127,128,130–134] for C. But for carbon the situation is rather complex because there are different structural forms of a carbon solid having varied density values. Fig. 8(c) shows that the experimental data measured by different researchers on carbon are very different. The main reason for this is considered to be due to the sample preparation, where the information about the sample, especially the form and the density of the sample, was not given in the literature in most cases. Below 2 keV Sternglass's data values [131] are very low while Bronshtein's data values [15] are rather high, and El-Gomati's data values [133] are moderate and are almost constant between 300 eV and 5 keV. El-Gomati et al. [133] further demonstrated that as expected the surface cleaning by ion bombardment alters the $\eta$ values very slightly since the contamination is mostly hydrocarbons.

Therefore, we have performed calculations for three typical carbon allotropes with the known density values given in Table 1. Fig. 8(c) shows that graphite has the lowest backscattering coefficients and amorphous carbon has the largest values, while the glassy carbon presents the intermediate backscattering coefficient values which agree excellently well with Bronshtein's experimental data [15] at low primary energies below 1 keV and are quite close to other experimental data at higher energies. It is also interesting to note from Table 1 and Fig. 8(c) that the graphite has higher density but lower $\eta$ values than glassy carbon, which should not be realistic. This is because, on the one hand, the crystalline form affects the electronic excitation as displayed by ELF in Fig. 3. On the other hand, the sum rules are strongly underestimated for boron and amorphous carbon indicating the underestimation of inelastic cross section, and are strongly overestimated for graphite indicating the overestimation of inelastic cross section. Fig. 5 shows that graphite has the smaller IMFP, and also the ratio $\lambda_{in}/\lambda_e$, as compared with glassy and amorphous carbon. Therefore, in Monte Carlo simulation electrons suffer much more inelastic events and less elastic scattering events in graphite than in glassy carbon. This explains why the simulated $\eta$ values are lower for heavier carbon (graphite) than the lighter glassy carbon and amorphous carbon. Because the ELF used for glassy carbon has quite satisfactory sum rule values, the simulated backscattering coefficients for glassy carbon should be much more reliable than amorphous carbon and graphite. Then, the simulation in agreement with Bronshtein's data [15] in the lower energy region below 1 keV and other experimental data in the higher energy region above 5 keV is quite reasonable.

Fig. 8(d) also illustrates the comparison with other reported Monte Carlo simulations on carbon [129,135–139] by using different simulation models and codes, mostly employed the stopping power equation in the continuous slowing down approximation for electron inelastic scattering. But this approximation is believed to be much poorer than the present individual inelastic scattering simulation based on a dielectric functional formalism, which describes the specific electronic excitation channel in a material rather than the simple $Z$-dependence in stopping power equation, particularly considering the fact that the Bethe stopping power equation is invalid at low energies and one has to introduce the modified mean ionization energy value. Depending on different approaches to stopping power equation, some of these codes yielded extreme low $\eta$ values. e.g. by NISTMonte [137] and Geant4 [139] codes, while others presented extreme high values at low energies [20].

Furthermore, Fig. 8(e) compares our simulated values with those calculated from Reuter's empirical fitting formula for high energy backscattering coefficients [140],$\eta = -0.0254 + 0.016Z - 1.86\times10^{-4}Z^2 + 8.3\times10^{-7}Z^3$, is given at 20 keV for Be, B and C. Our present simulation also agrees well with the formula for B and C, and slightly smaller for Be.

Looking at experimental data solely, an obvious character of Bronshtein's data [15] for Be and C in comparing with others is that the $\eta(E_p)$ curve has a maximum around several hundred eV but not monotonously increasing when primary energy $E_p$ is reduced. The tendency agrees well with the present calculation. The clue from this observation is that the reason for the uncertainty involved in experimental data can be partly accounted for. Experimentally the effects of surface roughness and cleanness existed in all experiments can affect the obtained results more or less. Like aluminum, beryllium is easy to be oxidized. Moreover, the presence of a surface carbonaceous layer on the specimen surface may also have a significant influence. The measurement performed without ultrahigh vacuum condition and ion beam sputtering would inevitably involve surface contamination due to residual gases containing hydrocarbon, carbon dioxide, oxygen and water molecules on a surface [141]. By vacuum baking and electron beam irradiation these adsorbed molecule species may change their structure or even dissociate into carbon, hydrogen, oxygen and even silicon atom species. Carbon, oxygen and silicon atoms have a large effect for increasing the $\eta$ value of bulk beryllium. It would be quite reasonable to consider that the higher $\eta$ values of experimental data than our calculation come mainly from surface contamination. The Drescher's [126] and Reimer's [14] data were measured in a scanning electron microscope without in situ surface cleaning procedure, and the samples

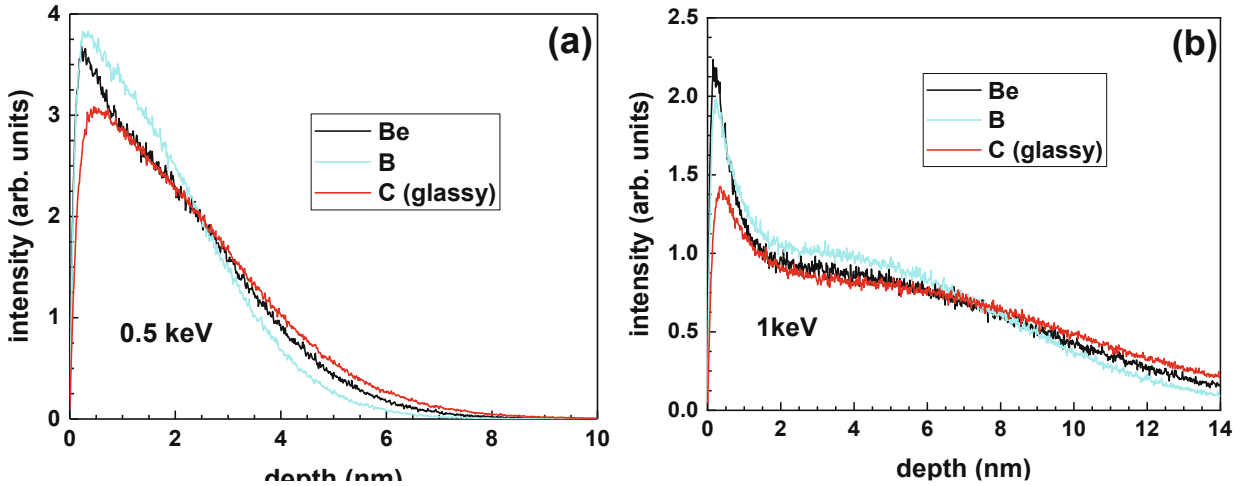


**Fig. 9.** Backscattered electron intensity as a function of maximum penetration depth for a normal incident electron beam of (a) 0.5 keV and (b) 1 keV. The distribution is normalized by the area under the curve.

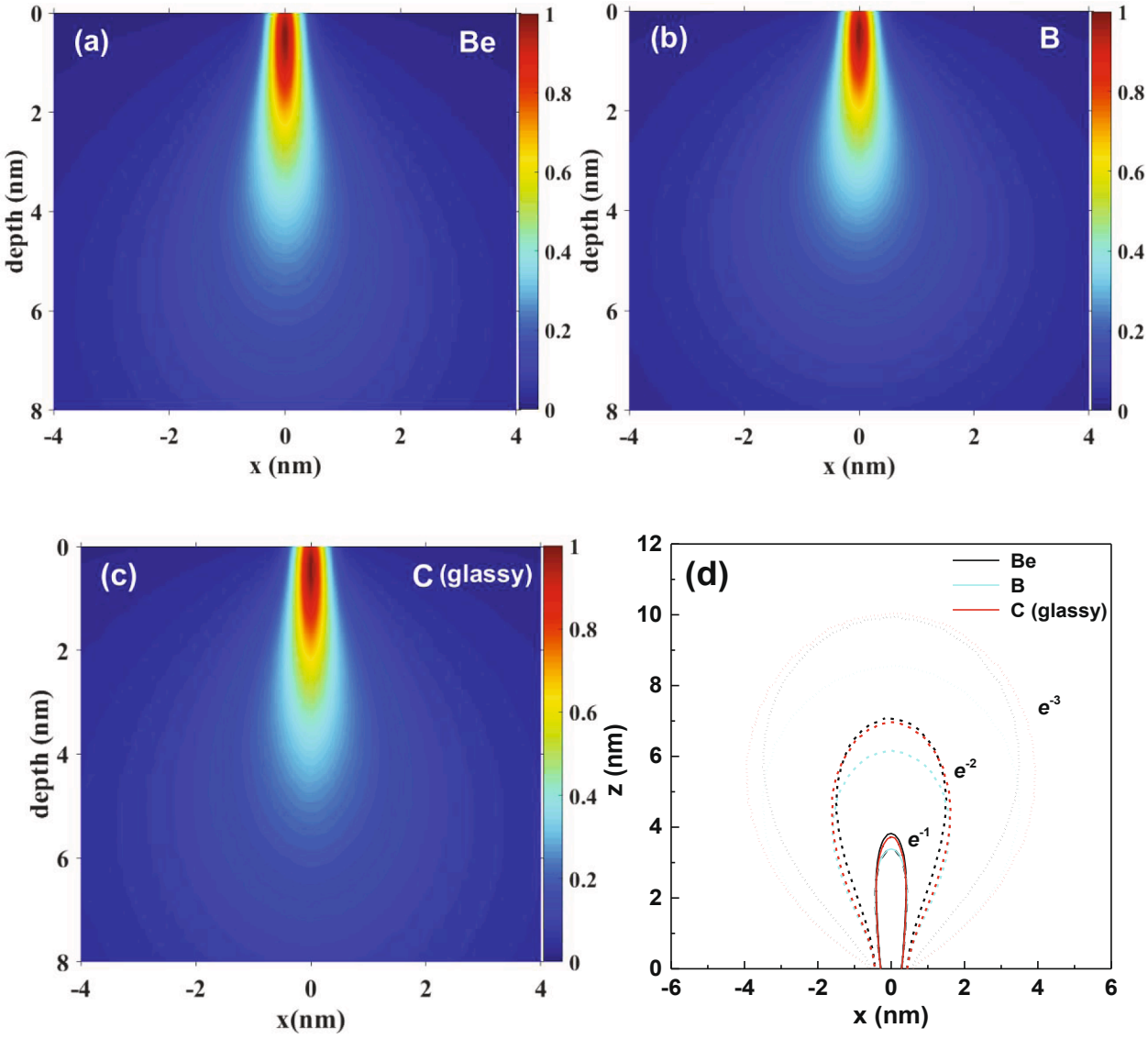


**Fig. 10.** Monte Carlo simulated relative intensity map of the electron trajectory spatial distribution for a normal incident electron beam of 0.5 keV: (a) Be, (b) B, (c) C (glassy). (d) A comparison of contour map for the three materials.

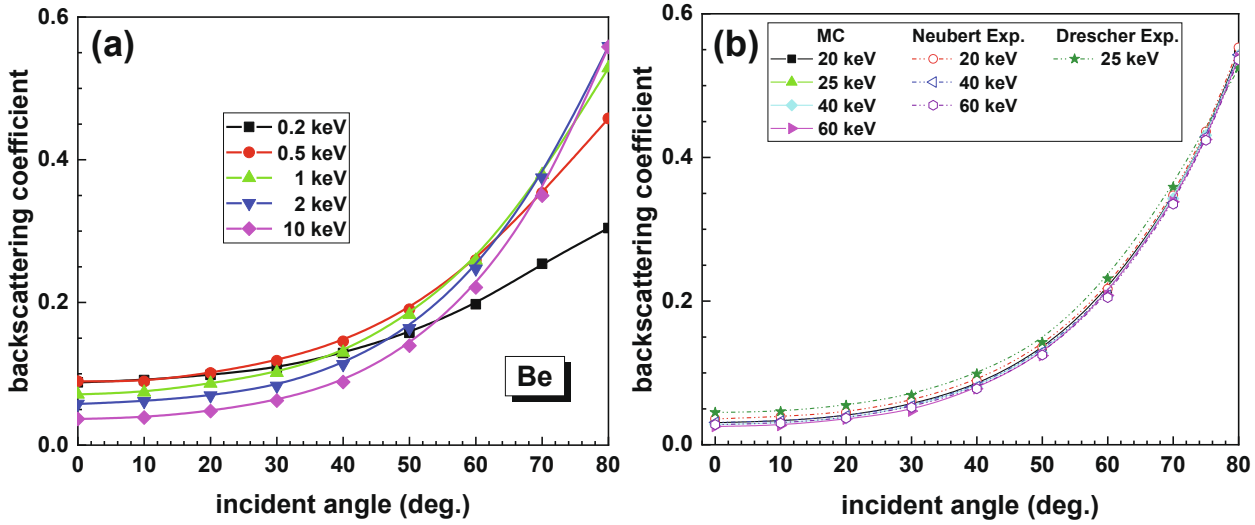


**Fig. 11.** Backscattering coefficients of Be as a function of incident angle with respect to the surface normal at different incident energies: (a) 0.2–10 keV; (b) 20–60 keV for comparison with experiments.

include electropolished metals, evaporated films and mechanically polished specimens. It is then not surprising that their data defines the upper limit of experimental data distribution range of beryllium. Shimizu had performed the measurement in an ultrahigh vacuum with an argon ion bombardment of the sample [16], and his data are lower than that of Reimer at high energies and approaches the data of Reimer when primary energy is lowered down to 1 keV. The sample property was not described in the Neubert's experiment [127]. Bronshtein et al. had prepared pristine beryllium surface by vacuum deposition of thin beryllium layers of various thicknesses onto a platinum substrate, and the target was heated to a high temperature for degassing [15]. The sample cleanness in this experiment explains why the Bronshtein's data are much lower than others.

Therefore, the surface cleanness can be one of the most responsible reasons of the disagreement between our calculation and experimental results. Because the physical properties, e.g. optical constants, of these complex adsorbates is generally unknown, we will consider in this work the contaminates made of amorphous carbon and water. Amorphous carbon is the dominate contamination ingredient as experimentally found, whose electrical properties has been measured by X-ray photoelectron spectroscopy [142] and whose optical data are available. For water its optical data are also available in the photon energy range of $1.24 \times 10^{-7} - 3 \times 10^{4}$ eV [36], while its optical data in the energy range of 30 keV-100 keV can be determined from the atomic scattering factor of H and O [112]. Therefore, we have performed another simulation for a bulk Be solid whose surface is either covered with an amorphous carbon or water layer with varying thickness. The simulation method for this contamination layer covered sample uses CTMC-ATOMIC, which is

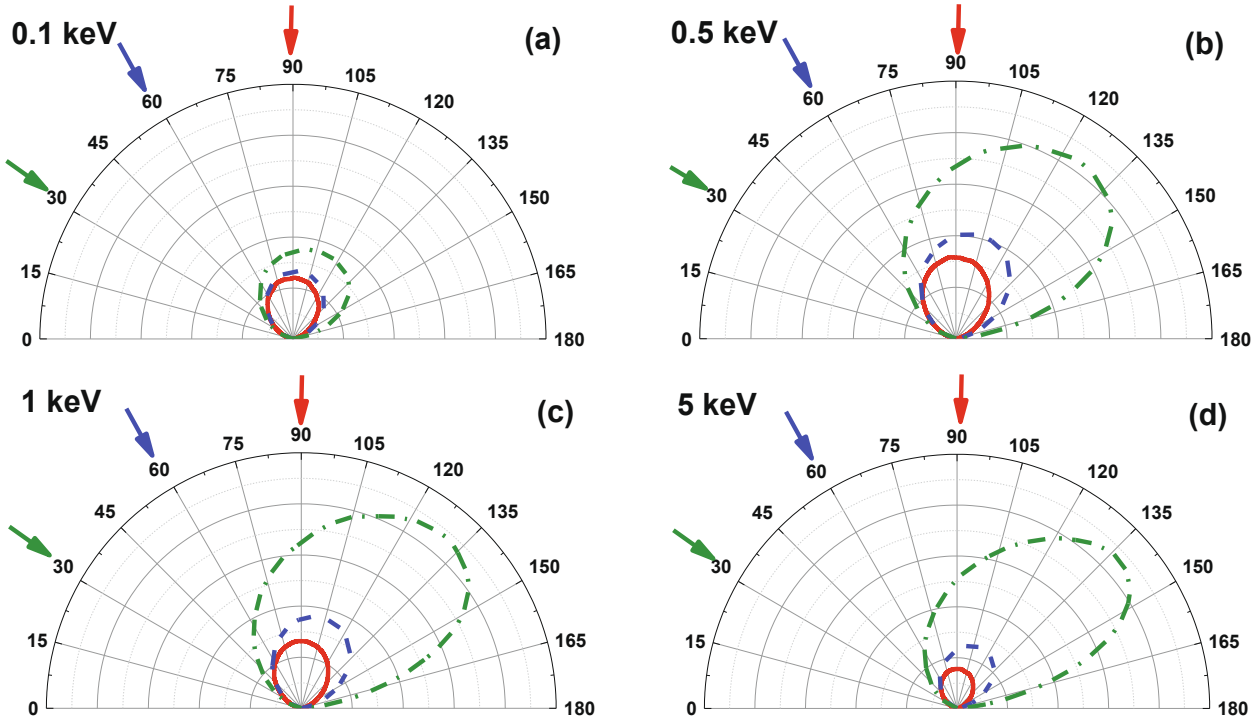


**Fig. 12.** Angular distributions of backscattered electrons of Be at several different incident angles, i.e. 30° (green), 60° (blue) and 90° (red), and primary energies: (a) 0.1 keV, (b) 1 keV, (c) 3 keV and (d) 5 keV.

basically the same as our previous Monte Carlo simulation of reflection electron energy loss spectrum for carbon contaminated sample by a surface excitation model [63], the difference is only that the present Monte Carlo model as described above is just a bulk excitation model because here we are not interested in weak surface excitation features near the elastic peak. The simulation results shown in Fig. 8(f) & 8(g) indeed indicate the trend of increasing the value at low primary energies below 1 keV by absorption of carbon layer and water layer, respectively; two carbon layers or one water layer are most likely existed in Bronshtein's sample [15]. This simulation explains very well part of the experimental data. Furthermore, additional existence of residual oxygen and silicon atoms on beryllium surface from decomposition of trisiloxanes actually will further enhance the contamination effect and even at high primary energies because their atomic numbers are greater than carbon. Hydrogen atoms will slightly weaken the commination effect because of the smaller atomic number and elastic scattering cross section compared with that of carbon. It has been also suggested by El-Gomati et al. that great care is needed in surface preparation at low primary beam energies for accurate $\eta$ determination [11].

To understand the mechanism leading to the $Z$-dependence of backscattering coefficients in more detail, we consider that the electron penetration spatial region, i.e. the interaction volume, may present some useful information. Fig. 9 shows the distributions of backscattered electron intensity on the maximum penetration depth at primary energies of 0.5 keV and 1 keV for three elemental solids. In the deep interior of the solid electrons have no enough energy to escape from the surface to be backscattered electrons. Therefore, the larger distribution range and smaller mean depth value estimated from the distribution for the lighter elements and at the higher primary energies indicate the lower $\eta$ values. Fig. 10 demonstrates the electron trajectory spatial distributions for three elemental solids. The colour scale from red to blue shows the intensity of the electron trajectory spatial distribution from high value to low value. The intensity is normalized by the number of the incident electrons. The contour lines in Fig. 10(d) represent the normalized intensities having values of $e^{-1}$, $e^{-2}$ and $e^{-3}$, for different degrees of attenuation according to natural logarithm. The diffusion rate can be seen from these contour lines. The broad distribution in horizontal direction represents the larger scattering angles in electron elastic scattering events and hence the larger $\eta$ values. This spatial distribution is determined by the combination effect of differential elastic scattering cross section (Fig. 1), elastic mean free path (Fig. 2(b)) and inelastic mean free path (Fig. 5(a)) while the latter two are related to material density. Cross section for electron elastic scattering with atoms depends on $Z$, but not monotonically. Fig. 2(a) shows that at higher energies, cross section is larger for the heavier element (C) than the lighter element (Be), and at lower energies it is reversed; the transition happens around 300–400 eV, which coincides with the energy $E_p$ for the maximum $\eta$. But after considering the density factor, the behaviour of elastic mean free path $\lambda_e$ is not a simple relation of $Z$, e.g. solid carbon has different forms and densities. The density also affects the value of inelastic mean free path $\lambda_{in}$ simultaneously. Therefore, instead of considering the $Z$-dependence only from $\lambda_e$ one has to consider the ratio $\lambda_{in}/\lambda_e$ (Fig. 5(b)). The greater $\lambda_{in}$ and smaller $\lambda_e$, the more elastic collisions than inelastic collisions and, hence, the larger the value of $\eta$. But, as it can be seen in Fig. 5(b) that this ratio is bigger for Be than C below 300–400 eV. Therefore, we must consider electron differential scattering cross section. For the lighter element Be, its forward elastic scattering is much stronger than the heavier element C; then electrons undergo more frequent small angle scattering in Be than in C. In fact, all these factors, i.e. total and differential scattering cross sections (both elastic and inelastic), together contribute to the smaller $\eta$ values of Be.

We have also calculated backscattering coefficients as functions of incident angle and emission angle. Fig. 11 shows the incident angle dependence for Be at several primary energies, and the comparison with experiment. The $\eta$ value increases with the incident angle, defined as the angle of electron beam with respect to the surface normal. This is because at lower incident angles, most of electrons are going deeper inside the materials and are more difficult for them to escape back from the material surfaces. The comparison of the simulation with the Neubert's experimental data [127] at incident energies of 20, 40 and 60 keV all fit very well in Fig. 11(b), where the Drescher's experimental data [126] for 25 keV incident energy are also displayed.

As results of our Monte Carlo simulations we can also evaluate the emission angular distributions of the backscattered electrons. Fig. 12 shows the simulated angular distributions of back scattered electrons at different incident angles and primary energies. Other than the total yield of backscattered electrons in Fig. 11, this figure displays how the emission angular distribution changes with the incident angle. Because beryllium is a light element and forward scattering is strong, then the emission maximum appears in the forward angular region, but not symmetrical about surface normal. The angular position for the maximum shifts with incident energy.

## 4. Conclusions

In this work, we have presented a Monte Carlo simulation of the electron backscattering coefficient of Be, B and C (glassy, graphite and amorphous) at impact energy range between 0.1 keV and 100 keV. Both the high energy cascade secondary electrons and Auger electrons produced during the transport of the incident electrons inside the bulk beryllium were taken into account. This up-to-date CTMC-SEM modelling uses the Mott's cross section calculated with more accurate scattering potential and a relativistic dielectric functional formalism with full Penn algorithm and experimental optical data. Sum rule checks indicate that, beryllium and glassy carbon have good sum rule values and the simulation of backscattering coefficients for them should be reasonable; while boron and amorphous possess an underestimated sum rule and graphite has overestimated ones, hence, the calculation of backscattering coefficients for them would tend to be overestimated and underestimated, respectively. The simulation results show that the Auger electrons contribute negligibly to the backscattering coefficient. For beryllium the simulation results are found well below experimental data at low energies and approaches the lower limit of the experimental data distribution range at high energies above 10 keV. Further simulations for carbon or water absorbed on beryllium surfaces indicate that a contamination with a thickness of one or two atomic/molecular layers can largely increase the backscattering coefficient of beryllium below 1 keV. Therefore, the early experimental data measured either in bad vacuum conditions and/or without previous ion-sputter cleaning of the surface are likely to be overestimated. The very low values of the backscattering coefficients for extreme low-Z elements (Be and B) are partly attributed to the strong elastic forward scattering, while previously it was assumed that the backscattering coefficient is dominated by the total cross sections of elastic and inelastic scattering. We believe we have derived the presently most accurate backscattering coefficients for beryllium and glassy carbon among all available theoretical and experimental data. We highly recommend to use these data in applications at least until further accurate experimental data for clean Be surface become available. Both reliable experimental and theoretical benchmark results need to be established in future.

## CRediT authorship contribution statement

**Abrar Hussain:** Investigation, Visualization, Writing - original draft. **Lihao Yang:** Methodology, Software, Validation, Writing - original draft. **Shifeng Mao:** Methodology, Software, Supervision. **Bo Da:** Methodology, Supervision. **Károly Tőkési:** Conceptualization, Writing - review & editing, Supervision. **Z.J. Ding:** Conceptualization, Software, Validation, Resources, Writing - review & editing, Supervision, Project administration, Funding acquisition.

## Declaration of Competing Interest

The authors declare that they have no known competing financial

interests or personal relationships that could have appeared to influence the work reported in this paper.

**Acknowledgements**

The work was supported by the National Key Research and Development Project (2019YFF0216404) and Education Ministry through "111 Project 2.0" (BP0719016), the National Research, Development and Innovation Office (NKFIH) under Grant KH126886 and the European Cost Actions CA15107 (MultiComp). This work at National Institute for Materials Science was supported by Grant for Basic Science Research Projects from the Sumitomo Foundation. We thank also Dr. H.M. Li and the supercomputing center of USTC for the support of parallel computing.

## 6. Appendix A: uncertainty analysis

Quantification of the computed data quality has been assessed by uncertainty. Recently the estimation of the uncertainty of the computer simulated results is becoming an important issue [143,144]. The sources of uncertainty for electron scattering calculations have been considered in Ref. [144]; following the general consideration on the uncertainty classification, the expression for the combined standard uncertainty [145] of the simulated backscattering coefficient can be expressed here as:

$$u^2_{\text{simulation}} = u^2_{\text{modelling}} + u^2_{\text{numerical}} + u^2_{\text{specimen}} \tag{A1}$$

where the three terms are due to physical modelling, numerical calculation and specimen parameters.

The uncertainty due to numerical calculation mainly originates from two parts, i.e. statistical fluctuation and the general computation uncertainty:

$$u^2_{\text{numerical}} = u^2_{\text{statistical}} + u^2_{\text{computation}} \tag{A2}$$

The statistical fluctuation term is given by $u_{\text{statistical}} \propto 1/\sqrt{N}$, where $N$ is the number of samples, i.e. the number of incident electrons here, which can be omitted in this work because $1\times10^8$ primary electron trajectories have been used in a simulation. The general computation uncertainty term, $u_{\text{computation}}$, is usually caused by the truncation error and the finite precision of computations with floating-point numerals. It has been shown that the incorrect interpolation process between the tabulated elastic cross section values can cause even larger effect, an obvious deviation on the simulation results [11]. All these factors have been carefully considered in our CTMC-SEM code and this uncertainty term is also negligible.

The specimen term, $u_{\text{specimen}}$, is caused by the uncertainties of the parameters used for describing the physical properties of the specimen, such as, mass density, work function, Fermi energy etc. These parameters are usually well defined for most of materials, and particularly, electron backscattering is not sensitive to work function. While some exceptions do exist, for example, the density of amorphous carbon has a rather large value range in between 1.4-3.0 g/cm$^3$ [146,147], which varies with the ways of production. The carbon layer covered on the Be specimen in the experiment is amorphous, whose density should be related to the particular experimental condition rather than a fixed value. As ELF is also related to the mass density, while it is known for amorphous carbon only for the density of 2.1 g/cm$^3$, which is the value we used for calculations of bulk amorphous carbon and carbon contaminated beryllium surface. Of course, the denser the amorphous carbon is the stronger the contamination effect will be. As for clean Be, the specimen term of uncertainty, $u_{\text{specimen}}$, is negligible. It can be understood from our discussions given above, the change of the $\eta$ value by contamination in a certain experiment should be attributed to the experimental uncertainty but not to the effect of theoretical simulation.

The uncertainty term due to physical modelling, $u_{\text{modelling}}$, is considered to be the most important term. It is composed of two parts here as,

$$u^2_{\text{modelling}} = u^2_{\text{elastic}} + u^2_{\text{inelastic}} \tag{A3}$$

where $u_{\text{elastic}}$ and $u_{\text{inelastic}}$ represent the uncertainties involved in a particular modelling of elastic and inelastic scattering, respectively. The Mott's cross section and dielectric functional theory (FPA) are regarded as the most accurate models for the description of electron elastic and inelastic scattering, respectively, up to now (see Appendix-B for a comparison with several other other approaches). However, the inputs to the calculations of Mott's cross section and IMFP, i.e. the scattering potential and the ELF, respectively, may still contain some uncertainties.

The deviation of ELF can be estimated by the errors of sum rules (see Table 2), which confirm that the $u_{\text{inelastic}}$ term is negligible for beryllium and glassy carbon. On the other hand, the scattering potential may have an impact on the calculated Mott's cross section and, hence, the simulation results of backscattering coefficient. In ELSEPA code the details for the calculation of elastic cross section are specified by the input arguments which are listed in part in Table A1 for the arguments, MNUCL, MELEC, MEXCH and MCPOL with their detailed description about the options [96]. A label "abcd" is used to denote the scattering potential, i.e. "MNUCL=a", "MELEC=b", "MEXCH=c", and "MCPOL=d". Note that the nuclear charge distribution will affect the calculated elastic cross section only for projectiles with kinetic energies higher than 50 MeV [96]. In this work, "MNUCL=3" is used and we will only focus on the influence of options for electron distribution model (MELEC), electron exchange potential (MEXCH) and electron correlation-polarization potential (MCPOL). Then totally 48 ($4\times4\times3$) different combinations of scattering potentials have been employed to calculate the uncertainty range of the elastic cross section.

Fig. A1(a) shows the range of total elastic scattering cross section as a function of electron energy as determined from 48 different scattering potentials. The "3412" curve is the total elastic scattering cross section used in present work, while the grey area represents the maximum error range calculated based on all other scattering potentials for free Be atom by using ELSEPA code [96]. Potential "3200" will lead to the smallest total elastic scattering cross section, and the potentials "3111", "3121" and "3131" will lead to the maximum ones. Fig. A1(b) shows the corresponding backscattering coefficient by using different Mott's cross sections shown in Fig. A1(a). As the full range from minimum to maximum values are considered the error is within 100% confidence limits. It can be seen that even with the largest elastic cross section, the calculated backscattering coefficients for pure Be are still much lower than the experimental data. This fact indicates that the uncertainty involved in the present Monte Carlo modelling has less effect to the conclusions made.

**Table A1**
part of the input arguments in the calculation of elastic cross section by ELSEPA code. For more details, please refer to Ref. [96].

| Argument | Values | Description |
|---|---|---|
| MNUCL | | Nuclear charge distribution model |
| | 1 | Point nucleus (P). |
| | 2 | Uniformly charged sphere (U). |
| | 3 | Fermi distribution (F). |
| | 4 | Helm's uniform-uniform distribution (Uu). |
| MELEC | | Electron distribution model |
| | 1 | Thomas-Fermi-Molière distribution (TFM). |
| | 2 | Thomas-Fermi-Dirac distribution (TFD). |
| | 3 | Dirac-Hartree-Fock-Slater distribution (DHFS). |
| | 4 | Numerical Dirac-Fock distribution (DF), read from the database files. |
| MEXCH | | Electron exchange potential |
| | 0 | No exchange potential. |
| | 1 | Furness-McCarthy potential (FM). |
| | 2 | Thomas-Fermi potential (TF). |
| | 3 | Riley-Truhlar potential (RT). |
| MCPOL | | Correlation-polarization potential |
| | 0 | No correlation-polarization potential. |
| | 1 | Buckingham potential (B). |
| | 2 | Local-density approximation (LDA). |

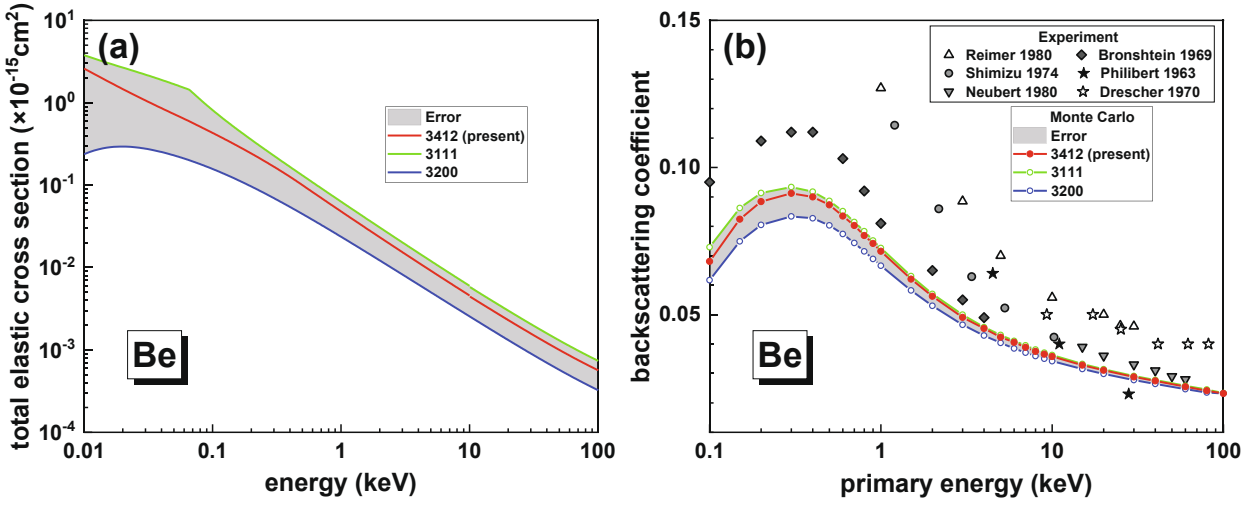


**Fig. A1.** Ranges of (a) total elastic cross section and (b) backscattering coefficient for beryllium for 100% confidence limits as determined from different scattering potentials.

## 7. Appendix B: comparison with other models

In addition to the models adopted in this work, i.e. the Mott's cross section and dielectric functional approach (FPA), there are some other theoretical models or approaches used for the description of electron elastic and inelastic scattering in a Monte Carlo simulation. Here we select several typical combinations of modelling [50] to investigate the sensitivity of backscattering coefficient to models [45]. Due to its simple analytical form, the screened Rutherford cross section had been widely used to describe elastic electron-atom collisions in the early years. The screened Rutherford differential scattering cross section is expressed by

$$\frac{d\sigma}{d\Omega} = \frac{Z^2 e^4}{4E^2(1 - cos\theta + 2\beta)^2} \tag{A4}$$

where $\beta$ is the atomic screening parameter, and is given by $\beta = 2.61Z^{2/3}/E$ where $E$ is in eV [148,149].

On the other hand, the continuous slowing down approximation (CSDA) with the use of stopping power formula, either Bethe's equation, Eq. (22), or the empirically modified expression [120], has been also widely used in a Monte Carlo modelling of electron inelastic scattering for various calculations including backscattering coefficient [150]. Fig. B1 illustrates the comparison on the electron backscattering coefficients of beryllium with different models for electron elastic and inelastic scattering. Here the stopping power in CSDA approach is obtained from our present FPA modelling as shown in Fig. 6. It is very clear that the use of screened Rutherford formula overestimates the backscattering coefficient, mostly due to the incorrect description of differential cross section, and, the CSDA approach underestimates the backscattering coefficient.

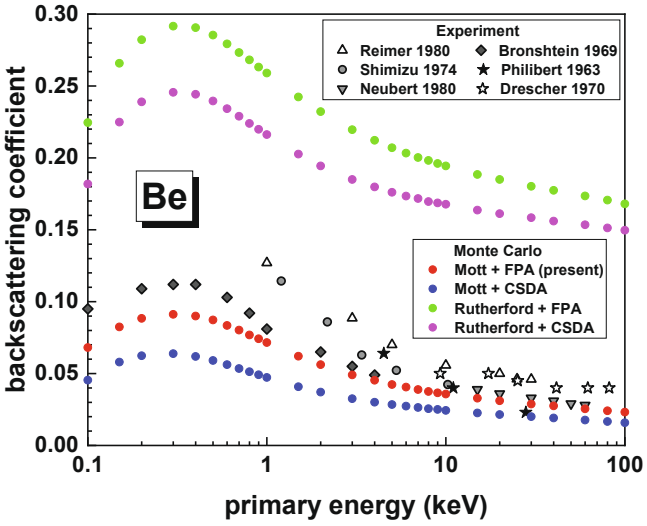


**Fig. B1.** Comparison on the electron backscattering coefficients of beryllium with different models for elastic collision and inelastic collision.

## References


[1] R. Aymar, P. Barabaschi, Y. Shimomura, The ITER design, Plasma Phys. Control. Fusion 44 (2002) 519–565.
[2] G. Federici, C.H. Skinner, J.N. Brooks, J.P.C. Coad, A.A. Haasz, A.V. Hassanein, C. S. Pitcher, J. Roth, W.R. Wampler, D.G. Whyte, Plasma material interactions in current tokamaks and their implications for next step fusion reactors, Nucl. Fusion 41 (2001) 1967–2137.
[3] P. Tolias, On electron backscattering from dust grains in fusion plasmas, Plasma Phys. Control. Fusion 56 (2014), 045003.
[4] L. Reimer, Image Formation in Low-voltage Scanning Electron Microscopy, vol. 12, SPIE press, 1993.
[5] H. Niedrig, Electron backscattering from thin films, J. Appl. Phys. 53 (1982) R15–R49.
[6] L. Reimer, Scanning Electron Microscopy: Physics of Image Formation and Microanalysis, vol. 45, Springer, 2013.
[7] H. Kim, T. Negishi, M. Kudo, H. Takei, K. Yasuda, Quantitative backscattered electron imaging of field emission scanning electron microscopy for discrimination of nano-scale elements with nm-order spatial resolution, J. Elect. Microsc. 59 (2010) 379–385.
[8] H.J. Hunger, L. Küchler, Measurements of the electron backscattering coefficient for quantitative EPMA in the energy range of 4 to 40 keV, Phys. Status Solidi 56 (1979) K45–K48.
[9] C. Merlet, Accurate description of surface ionization in electron probe microanalysis: an improved formulation, X-Ray Spectrom. 21 (1992) 229–238.
[10] E. Darlington, V. Cosslett, Backscattering of 0.5-10 keV electrons from solid targets, J. Phys. D Appl. Phys. 5 (1972) 1969.
[11] M. El Gomati, C. Walker, A. Assa'd, M. Zadražil, Theory experiment comparison of the electron backscattering factor from solids at low electron energy (250–5,000 eV), Scanning 30 (2008) 2–15.
[12] D. Joy, A database on electron-solid interactions, Scanning 17 (1995) 270–275.
[13] J.W. Martin, J. Yuan, S. Hoedl, B. Filippone, D. Fong, T. Ito, E. Lin, B. Tipton, A. R. Young, Measurement of electron backscattering in the energy range of neutron β decay, Phys. Rev. C 68 (2003), 055503.
[14] L. Reimer, C. Tollkamp, Measuring the backscattering coefficient and secondary electron yield inside a scanning electron microscope, Scanning 3 (1980) 35–39.
[15] I. Bronshtein, B.S. Fraiman, Secondary Electron Emission (in Russian), Nauka, Moskva, 1969, p. 340.
[16] R. Shimizu, Secondary electron yield with primary electron beam of kilo-electron-volts, J. Appl. Phys. 45 (1974) 2107–2111.
[17] L. Spencer, U. Fano, Energy spectrum resulting from electron slowing down, Phys. Rev. B 93 (1954) 1172.
[18] R. Shimizu, Z.J. Ding, Monte Carlo modelling of electron-solid interactions, Rep. Prog. Phys. 55 (1992) 487.
[19] D.C. Joy, Monte Carlo Modeling for Electron Microscopy and Microanalysis, Oxford Univ. Press, 1995.
[20] M. Dapor, Transport of Energetic Electrons in Solids: Computer Simulation with Applications to Materials Analysis and Characterization, Springer, 2016.
[21] Z.J. Ding, R. Shimizu, T. Sekine, Y. Sakai, Theoretical and experimental studies of N(E) spectra in Auger electron spectroscopy, Appl. Surf. Sci. 33 (34) (1988) 99–106.
[22] Z.J. Ding, R. Shimizu, Monte Carlo study of backscattering and secondary electron generation, Surf. Sci. 197 (1988) 539–554.
[23] Z.J. Ding, R. Shimizu, Inelastic collisions of kV electrons in solids, Surf. Sci. 222 (1989) 313–331.
[24] Z.J. Ding, R. Shimizu, Theoretical study of the ultimate resolution of SEM, J. Microsc. 154 (1989) 193–207.
[25] Z.J. Ding, R. Shimizu, K. Goto, Background formation in the low energy region in Auger electron spectroscopy, J. Appl. Phys. 76 (1994) 1187–1195.
[26] Z.J. Ding, T. Nagatomi, R. Shimizu, K. Goto, Monte Carlo simulation of background in AES: a comparison with experiment, Surf. Sci. 336 (1995) 397–403.
[27] Z.J. Ding, R. Shimizu, A Monte Carlo modeling of electron interaction with solids including cascade secondary electron production, Scanning 18 (1996) 92–113.
[28] Z.J. Ding, X.D. Tang, R. Shimizu, Monte Carlo study of secondary electron emission, J. Appl. Phys. 89 (2001) 718–726.
[29] Z.J. Ding, X.D. Tang, H.M. Li, Monte Carlo calculation of the energy distribution of backscattered electrons, Int. J. Mod. Phys. B 16 (2002) 4405–4412.
[30] Z.J. Ding, H.M. Li, X.D. Tang, R. Shimizu, Monte Carlo simulation of absolute secondary electron yield of Cu, Appl. Phys. A 78 (2004) 585–587.
[31] Z.J. Ding, H.M. Li, K. Goto, Y.Z. Jiang, R. Shimizu, Energy spectra of backscattered electrons in Auger electron spectroscopy: comparison of Monte Carlo simulations with experiment, J. Appl. Phys. 96 (2004) 4598–4606.
[32] S.F. Mao, Y.G. Li, R.G. Zeng, Z.J. Ding, Electron inelastic scattering and secondary electron emission calculated without the single pole approximation, J. Appl. Phys. 104 (2008), 114907.
[33] S.F. Mao, X. Sun, X.W. Fang, B. Da, Z.J. Ding, A Monte Carlo study of spin polarization of secondary electrons, Surf. Interface Anal. 44 (2012) 703–708.
[34] Y.B. Zou, S.F. Mao, B. Da, Z.J. Ding, Surface sensitivity of secondary electrons emitted from amorphous solids: calculation of mean escape depth by a Monte Carlo method, J. Appl. Phys. 120 (2016), 235102.
[35] C. Li, S.F. Mao, Z.J. Ding, Time-dependent characteristics of secondary electron emission, J. Appl. Phys. 125 (2019), 024902.
[36] Mehnaz, L.H. Yang, Y.B. Zou, B. Da, S.F. Mao, H.M. Li, Y.F. Zhao, Z.J. Ding, A comparative study on Monte Carlo simulations of electron emission from liquid water, Med. Phys. 47 (2020) 759–771.
[37] A. Hussain, L.H. Yang, Y.B. Zou, S.F. Mao, B. Da, H.M. Li, Z.J. Ding, Theoretical calculation of the mean escape depth of secondary electron emission from compound semiconductor materials, J. Appl. Phys. 127 (2020), 125304.
[38] A. Hussain, L.H. Yang, Y.B. Zou, S.F. Mao, B. Da, H.M. Li, Z.J. Ding, Monte Carlo simulation study of electron yields from semiconductor materials, J. Appl. Phys. 128 (2020), 015305.
[39] H.M. Li, Z.J. Ding, Monte Carlo simulation of secondary electron and backscattered electron images in scanning electron microscopy for specimen with complex geometric structure, Scanning 27 (2005) 254–267.
[40] Y.T. Yue, H.M. Li, Z.J. Ding, Monte Carlo simulation of secondary electron and backscattered electron images for a nanoparticle-matrix system, J. Phys. D Appl. Phys. 38 (2005) 1966–1977.
[41] H.M. Li, Z.J. Ding, A Monte Carlo simulation of secondary and backscattered electrons images of SEM, Acta Metall. Sin. 18 (2005) 351–355.
[42] Z.J. Ding, H.M. Li, Application of Monte Carlo simulation to SEM image contrast of complex structures, Surf. Interface Anal. 37 (2005) 912–918.
[43] Y.G. Li, S.F. Mao, H.M. Li, S.M. Xiao, Z.J. Ding, Monte Carlo simulation study of SEM images of rough surfaces, J. Appl. Phys. 104 (2008), 064901.
[44] Y.G. Li, Z.J. Ding, Z.M. Zhang, Monte Carlo simulation study of scanning Auger electron images, J. Appl. Phys. 106 (2009), 024316.
[45] J.S. Villarrubia, Z.J. Ding, Sensitivity of model-based SEM dimensional measurements to model assumptions, J. Micro/Nanolith. MEMS MOEMS 8 (2009), 033003.
[46] S.F. Mao, Z.J. Ding, A Monte Carlo simulation study on the image resolution in scanning electron microscopy, Surf. Interface Anal. 42 (2010) 1096–1099.
[47] P. Zhang, H.Y. Wang, Y.G. Li, S.F. Mao, Z.J. Ding, Monte Carlo simulation of secondary electron images for real sample structures in scanning electron microscopy, Scanning 34 (2012) 145–150.
[48] Y.G. Li, P. Zhang, Z.J. Ding, Monte Carlo simulation of CD-SEM images for linewidth and critical dimension metrology, Scanning 35 (2013) 127–139.
[49] Y.B. Zou, M.S.S. Khan, H.M. Li, Y.G. Li, W. Li, S.T. Gao, L.S. Liu, Z.J. Ding, Use of model-based library in critical dimension measurement by CD-SEM, Measurement 123 (2018) 150–162.
[50] Z.J. Ding, Z.Q. Wu, A comparison of Monte Carlo simulation of electron scattering and X-ray production in solids, J. Phys. D Appl. Phys. 26 (1993) 507–516.
[51] Z.J. Ding, Z.Q. Wu, Monte Carlo calculation of X-ray depth profiles in Si substrate coated with films, J. Phys. D Appl. Phys. 27 (1994) 387–392.
[52] Z.J. Ding, R. Shimizu, K. Obori, Monte Carlo simulation of X-ray spectra in electron probe microanalysis, J. Appl. Phys. 76 (1994) 7180–7187.
[53] Z.J. Ding, R. Shimizu, K. Goto, Intrinsic Auger signal profiles derived by Monte Carlo analysis, Appl. Surf. Sci. 100 (1996) 15–19.
[54] S.F. Mao, Z.M. Zhang, K. Tokesi, A. Csik, J. Toth, R.J. Bereczky, Z.J. Ding, XPS study of nano thin films on substrate, Surf. Interface Anal. 40 (2008) 728–730.
[55] N. Cao, B. Da, Y. Ming, S.F. Mao, K. Goto, Z.J. Ding, Monte Carlo simulation of full energy spectrum of electrons emitted from silicon in Auger electron spectroscopy, Surf. Interface Anal. 47 (2015) 113–119.
[56] D.S. You, H.M. Li, Z.J. Ding, Monte Carlo simulation of Auger electron emission from thin film on substrate, J. Electr. Spectrosc. Relat. Phenom. 222 (2018) 156–161.
[57] Z.J. Ding, Inelastic scattering of electrons at real metal surfaces, Phys. Rev. B 55 (1997) 9999–10013.
[58] Z.J. Ding, R. Shimizu, Monte Carlo simulation study of reflection electron energy loss spectroscopy spectrum, Phys. Rev. B 61 (2000) 14128–14135.

[59] Z.J. Ding, H.M. Li, Q.R. Pu, Z.M. Zhang, R. Shimizu, Reflection electron energy loss spectrum of surface plasmon excitation of Ag: a Monte Carlo study, Phys. Rev. B 66 (2002), 085411.

[60] Z.J. Ding, K. Salma, H.M. Li, Z.M. Zhang, K. Tokesi, D. Varga, J. Toth, K. Goto, R. Shimizu, Monte Carlo simulation study of electron interaction with solids and surfaces, Surf. Interface Anal. 38 (2006) 657–663.

[61] Y.G. Li, Z.M. Zhang, S.F. Mao, Z.J. Ding, Monte Carlo simulation study of quasi-elastic electron scattering from an overlayer/substrate system, J. Phys.: Condens. Matter 20 355005 (2008).

[62] B. Da, S.F. Mao, G.H. Zhang, X.P. Wang, Z.J. Ding, Monte Carlo modeling of surface excitation in reflection electron energy loss spectroscopy spectrum for rough surfaces, J. Appl. Phys. 112 (2012), 034310.

[63] B. Da, Z. Li, H. Chang, S.F. Mao, Z.J. Ding, A Monte Carlo study of reflection electron energy loss spectroscopy spectrum of a carbon contaminated surface, J. Appl. Phys. 116 (2014), 124307.

[64] X. Ding, B. Da, J.B. Gong, S.F. Mao, H.M. Li, Z.J. Ding, Quantification of surface roughness effect on elastically backscattered electrons, Surf. Interface Anal. 46 (2014) 489–496.

[65] J.M. Gong, L.H. Yang, K. Tőkési, Z.J. Ding, Surface and bulk excitations of silver determined from the reflected energy loss spectroscopy spectra, Eur. Phys. J. D 73 (2019) 24.

[66] B. Da, L.H. Yang, J.W. Liu, Y.G. Li, S.F. Mao, Z.J. Ding, Monte Carlo simulation study of reflection electron energy loss spectroscopy of a Fe/Si layered nanostructure, Surf. Interface Anal. (2020), https://doi.org/10.1002/sia.6864.

[67] B. Da, Y. Sun, S.F. Mao, Z.M. Zhang, H. Jin, H. Yoshikawa, S. Tanuma, Z.J. Ding, A reverse Monte Carlo method for deriving optical constants of solids from REELS spectra, J. Appl. Phys. 113 (2013), 214303.

[68] H. Xu, B. Da, J. Tóth, K. Tőkési, Z.J. Ding, Absolute determination of optical constants by reflection electron energy loss spectroscopy spectra, Phys. Rev. B 95 (2017), 195417.

[69] H. Xu, L.H. Yang, B. Da, J. Tóth, K. Tőkési, Z.J. Ding, Study of optical and electronic properties of nickel from reflection electron energy loss spectra, Nucl. Inst. Methods Phys. Res. B 406 (2017) 475–481.

[70] H. Xu, L.H. Yang, J. Tóth, K. Tőkési, B. Da, Z.J. Ding, Absolute determination of optical constants of three transition metals using reflection electron energy loss spectroscopy, J. Appl. Phys. 123 (2018), 043306.

[71] L.H. Yang, M. Menyhard, A. Sulyok, K. Tőkési, Z.J. Ding, Optical properties and excitation energies of iridium derived from reflection electron energy loss spectroscopy spectra, Appl. Surf. Sci. 456 (2018) 999–1003.

[72] L.H. Yang, K. Tőkési, J. Tóth, B. Da, H.M. Li, Z.J. Ding, Optical properties of silicon and germanium determined by high-precision analysis of reflection electron energy loss spectroscopy spectra, Phys. Rev. B 100 (2019), 245209.

[73] L.H. Yang, J. Tóth, K. Tőkési, B. Da, Z.J. Ding, Determination of electron inelastic mean free path of three transition metals from reflection electron energy loss spectroscopy spectrum measurement data, Eur. Phys. J. D 73 (2019) 21.

[74] C. Li, S.F. Mao, Y.B. Zou, Y.G. Li, P. Zhang, H.M. Li, Z.J. Ding, A Monte Carlo modeling on charging effect for structures with arbitrary geometries, J. Phys. D Appl. Phys. 51 (2018), 165301.

[75] C. Li, B. Da, Z.J. Ding, Monte Carlo study on the surface potential measurement using the peak-shift method, Appl. Surf. Sci. 504 (2020), 144138.

[76] C. Li, K. Tőkési, L. Repetto, L.X. Xiao, J.B. Liu, Z.S. Gao, L. Han, B. Da, Z.J. Ding, A Monte Carlo calculation on the secondary electron emission from a $SiO_2$ macro-capillary, Eur. Phys. J. D 74 (2020) 37.

[77] C. Li, H.M. Li, Z.J. Ding, Multiple coupled charge layers in electron beam induced charging phenomenon, J. Appl. Phys. 128 (2020), 024902.

[78] C. Li, B. Da, J.W. Liu, Z.J. Ding, Monte Carlo approach to charging induced by electron beam irradiation, Sci. Technol. Adv. Mater. (under revision).

[79] B. Da, J.W. Liu, M. Yamamoto, Y. Ueda, K. Watanabe, N.T. Cuong, S.L. Li, K. Tsukagoshi, H. Yoshikawa, H. Iwai, S. Tanuma, H.X. Guo, Z.S. Gao, X. Sun, Z. J. Ding, Virtual substrate method for nanomaterials characterization, Nat. Commun. 8 (2017) 15629.

[80] B. Da, Y. Sun, Z.F. Hou, J.W. Liu, N.T. Cuong, K. Tsukagoshi, H. Yoshikawa, S. Tanuma, J. Hu, Z.S. Gao, Z.J. Ding, Measurement of the low-energy electron inelastic mean free path in monolayer graphene, Phys. Rev. Appl. 13 (2020), 044055.

[81] H.T. Nguyen-Truong, B. Da, L.H. Yang, Z.J. Ding, H. Yoshikawa, S. Tanuma, Low-energy electron inelastic mean free path for monolayer graphene, Appl. Phys. Lett. 117 (2020), 033103.

[82] M. Zhang, Y. Ming, R.G. Zeng, Z.J. Ding, Calculation of Bohmian quantum trajectories for STEM, J. Microsc. 260 (2015) 200–207.

[83] L. Cheng, Y. Ming, Z.J. Ding, Bohmian trajectory-Bloch wave approach to dynamical simulation of electron diffraction in crystal, New J. Phys. 20 (2018), 113004.

[84] L. Cheng, Z.J. Ding, Novel quantum trajectory approaches to simulation of electron backscatter diffraction, J. Surf. Sci. Nanotech. 18 (2020) 121–125.

[85] Z. Ruan, M. Zhang, R.G. Zeng, Y. Ming, B. Da, S.F. Mao, Z.J. Ding, Simulation study of the atomic resolution secondary electron imaging, Surf. Interface Anal. 46 (2014) 1296–1300.

[86] Z. Ruan, R.G. Zeng, Y. Ming, M. Zhang, B. Da, S.F. Mao, Z.J. Ding, Quantum trajectory Monte Carlo method for study of electron-crystal interaction in STEM, Phys. Chem. Chem. Phys. 17 (2015) 17628–17637.

[87] L. Cheng, L.H. Yang, R.G. Zeng, Y. Ming, B. Da, Z.J. Ding, A robust quantum trajectory Monte Carlo simulation of atomic resolution secondary electron image (to be published).

[88] N.F. Mott, The scattering of fast electrons by atomic nuclei, Proc. R. Soc. Lond. A 124 (1929) 425–442.

[89] B. Hahn, D.G. Ravenhall, R. Hofstadter, High energy electron scattering and the charge distributions of selected nuclei, Phys. Rev. 101 (1956) 1131–1142.

[90] J. Desclaux, A multiconfiguration relativistic Dirac-Fock program, Comput. Phys. Commun. 9 (1975) 31–45.

[91] J.B. Furness, I.E. McCarthy, Semiphenomenological optical model for electron scattering on atoms, J. Phys. B: At. Mol. Phys. 6 (1973) 2280.

[92] D.R. Lide, CRC Handbook of Chemistry and Physics, Vol. 79, CRC Press, Boca Raton, FL, 1999.

[93] M.H. Mittleman, K.M. Watson, Effects of the Pauli principle on the scattering of high energy electrons by atoms, Ann. Phys. 10 (1960) 268–279.

[94] J.P. Perdew, A. Zunger, Self interaction correction to density functional approximations for many electron systems, Phys. Rev. B 23 (1981) 5048.

[95] F. Salvat, Optical-model potential for electron and positron elastic scattering by atoms, Phys. Rev. A 68 (2003), 012708.

[96] F. Salvat, A. Jablonski, C.J. Powell, ELSEPA Dirac partial-wave calculation of elastic scattering of electrons and positrons by atoms, positive ions and molecules, Comput. Phys. Commun. 165 (2005) 157–190.

[97] D.R. Penn, Electron mean-free-path calculations using a model dielectric function, Phys. Rev. B 35 (1987) 482.

[98] S. Tanuma, C.J. Powell, D.R. Penn, Calculations of electron inelastic mean free paths for 31 materials, Surf. Interface Anal. 11 (1988) 577–589.

[99] S. Tanuma, C.J. Powell, D.R. Penn, Dependence of inelastic electron mean free paths on electron energy and material, J. Vac. Sci. Technol. A 6 (1988) 1041–1042.

[100] S. Tanuma, C.J. Powell, D.R. Penn, Calculations of electron inelastic mean free paths. II. Data for 27 elements over the 50–2000 eV range, Surf. Interface Anal. 17 (1991) 911–926.

[101] S. Tanuma, C.J. Powell, D.R. Penn, Calculations of electron inelastic mean free paths: VIII. Data for 15 elemental solids over the 50–2000 eV range, Surf. Interface Anal. 37 (2005) 1–14.

[102] H. Shinotsuka, S. Tanuma, C.J. Powell, D.R. Penn, Calculations of electron inelastic mean free paths. X. Data for 41 elemental solids over the 50 eV to 200 keV range with the relativistic full Penn algorithm, Surf. Interface Anal. 47 (2015) 871–888.

[103] H. Shinotsuka, B. Da, S. Tanuma, H. Yoshikawa, C.J. Powell, D.R. Penn, Calculations of electron inelastic mean free paths. XI. Data for liquid water for energies from 50 eV to 30 keV, Surf. Interface Anal. 49 (2017) 238–252.

[104] H. Shinotsuka, S. Tanuma, C.J. Powell, D.R. Penn, Calculations of electron inelastic mean free paths. XII. data for 42 inorganic compounds over the 50 eV to 200 keV range, Surf. Interface Anal. 51 (2019) 427–457.

[105] X. Liu, Z. Hou, D. Lu, B. Da, H. Yoshikawa, S. Tanuma, Y. Sun, Z.J. Ding, Unveiling the principle descriptor for predicting the electron inelastic mean free path based on a machine learning framework, Sci. Technol. Adv. Mater. 20 (2019) 1090–1102.

[106] E.D. Palik, Handbook of Optical Constants of Solids, vol. 3, Academic Press, 1998.

[107] B. Henke, E. Gullikson, J. Davis, X-ray interactions: photoabsorption, scattering, transmission, and reflection at E = 50–30,000 eV, Z = 1-92, At. Data Nucl. Data Tables 54 (1993) 181–342.

[108] P. Prieto, C. Quiros, E. Elizalde, J.M. Sanz, Electron inelastic mean free path and dielectric properties of a-boron, a-carbon, and their nitrides as determined by quantitative analysis of reflection electron energy loss spectroscopy, J. Vac. Sci. Technol., A 24 (2006) 396–407.

[109] I. Abril, R. Garcia-Molina, C.D. Denton, F.J. Pérez-Pérez, N.R. Arista, Dielectric description of wakes and stopping powers in solids, Phys. Rev. A 58 (1998) 357.

[110] H. Venghaus, Redetermination of the dielectric function of graphite, Phys. Status Solidii (b) 71 (1975) 609–614.

[111] H.J. Hagemann, W. Gudat, C. Kunz, Optical constants from the far infrared to the x-ray region: Mg, Al, Cu, Ag, Au, Bi, C, and $Al_2O_3$, J. Opt. Soc. Am. 65 (1975) 742–744.

[112] D.E. Cullen, J.H. Hubbell, L. Kissel, EPDL97: The Evaluated Photo Data Library97 Version, Lawrence Livermore National Lab, CA (US), 1997.

[113] S. Tanuma, C.J. Powell, D.R. Penn, Use of sum rules on the energy-loss function for the evaluation of experimental optical data, J. Electr. Spectrosc. Relat. Phenom. 62 (1993) 95–109.

[114] D. Pines, P. Nozières, The Theory of Quantum Liquids: Superfluid Bose Liquids, Addison-Wesley, 1990.

[115] G.D. Mahan, Many-Particle Physics, Springer Science & Business Media, 2013.

[116] H. Bethe, Zur theorie des durchgangs schneller korpuskularstrahlen durch materie, Ann. Phys. 397 (1930) 325–400.

[117] H. Bethe, J. Ashkin, Experimental Nuclear Physics, Wiley, New York, 1953.

[118] M.J. Berger, S.M. Seltzer, Studies in Penetration of Charged Particles in Matter. Nuclear Science Series Report No. 39, NAS-NRC Publication No. 1133, National Academy of Science, Washington, DC 205, 1964.

[119] M.J. Berger, S.M. Seltzer, Tables of energy losses and ranges of electrons and positrons, NASA Special Publication 3012 (1964).

[120] D.C. Joy, S. Luo, An empirical stopping power relationship for low-energy electrons, Scanning 11 (1989) 176.

[121] A. Jablonski, S. Tanuma, C.J. Powell, New universal expression for the electron stopping power for energies between 200 eV and 30 keV, Surf. Interface Anal. 38 (2006) 76–83.

[122] H.T. Nguyen-Truong, Modified Bethe formula for low-energy electron stopping power without fitting parameters, Ultramicroscopy 149 (2015) 26–33.

[123] H. Shinotsuka, S. Tanuma, C.J. Powell, D.R. Penn, Calculations of electron stopping powers for 41 elemental solids over the 50 eV to 30 keV range with the full Penn algorithm, Nucl. Inst. Methods Phys. Res. B 270 (2012) 75–92.

[124] J.A.D. Matthew, in: Scanning Auger Electron Microscopy, John Wiley & Sons, New York, 2006, pp. 15–44.
[125] G. Love, V.E. Scott, Evaluation of a new correction procedure for quantitative electron probe microanalysis, J. Phys. D Appl. Phys. 11 (1978) 106.
[126] H. Drescher, L. Reimer, H. Seidel, Backscattering and secondary electron emission of 10–100 keV electrons in scanning electron microscopy, Z. Angew. Phys. 29 (1970) 331–336.
[127] G. Neubert, S. Rogaschewski, Backscattering coefficient measurements of 15 to 60 keV electrons for solids at various angles of incidence, Phys. Status Solidii (a) 59 (1980) 35–41.
[128] J. Philibert, E. Weinryb, in: Proc. 3rd Int. Conf. X-ray Opt. Microanal., Academic, New York, 1963, p. 163.
[129] S. Tanuma, An improved backscattering correction equation for wide analytical conditions on quantitative Auger analysis, J. Surf. Anal. 15 (2009) 312–316.
[130] K.F.J. Heinrich, in: X-ray Opt. & X-ray Microanal., Hermann, Paris, 1966, p. 159.
[131] E.J. Sternglass, Backscattering of kilovolt electrons from solids, Phys. Rev. 95 (1954) 345.
[132] P.C.R.E. Palluel, Electronique composante rediffusee du rayonnement electronique secondaire des metaux, C. R. Seances Acad. Sci. 224 (1947) 1492–1494.
[133] M. El-Gomati, C. Walker, X. Zha, Towards quantitative scanning electron microscopy: applications to nano-scale analysis, Nucl. Inst. Methods Phys. Res. A 645 (2011) 68–73.
[134] H.E. Bishop, Electron scattering and X-ray production (Ph.D. Thesis), University of Cambridge, UK, 1966.
[135] F. Salvat, J.M. Fernández-Varea, J. Sempau, ENELOPE-2006: a code system for Monte Carlo simulation of electron and photon transport, in: Workshop Proceedings, (Barcelona, Spain) 30 Jun.-3 Jul., 7, 2006.
[136] H. Demers, P. Horny, R. Gauvin, E. Lifshin, WinX-ray: a new Monte Carlo program for the simulation of X-ray and charging materials, Microsc. Microanal. 8 (2002) 1498–1499.
[137] N.W.M. Ritchie, A new Monte Carlo application for complex sample geometries, Surf. Interface Anal. 37 (2005) 1006–1011.
[138] Y. Lin, D.C. Joy, A new examination of secondary electron yield data, Surf. Interface Anal. 37 (2005) 895–900.
[139] S.H. Kim, M.G. Pia, T. Basaglia, M.C. Han, G. Hoff, C.H. Kim, P. Saracco, Validation test of Geant4 simulation of electron backscattering, IEEE Trans. Nucl. Sci. 62 (2015) 451–479.
[140] J. Goldstein, D.E. Newbury, D.C. Joy, C.Z. Lyman, P. Echlin, E. Lifshin, L. Sawyer, J.R. Michael, Scanning Electron Microscopy and X-ray Microanalysis, Springer, 2003.
[141] C.F. Mallinsonz, J.F. Watts, Effect of hydrocarbon contamination on the volta potential of second phase particles in beryllium, J. Electrochem. Soc. 163 (2016) C420–C422.
[142] S.H. Jun, K.Y. Jin, K. Jongkuk, K.D. Hyeong, H.S. Been, K.S. Jun, K.H. Ki, Tetrahedral amorphous carbon prepared filter cathodic vacuum arc for hole transport layers in perovskite solar cells and quantum dots LEDs, Sci. Technol. Adv. Mater. 20 (2019) 1118–1130.
[143] J. Sacks, W.J. Welch, T.J. Mitchell, H.P. Wynn, Design and analysis of computer experiments, Stat. Sci. 4 (1989) 409–423.
[144] H.K. Chung, B.J. Braams, K. Bartschat, A.G. Császár, G.W.F. Drake, T. Kirchner, V. Kokoouline, J. Tennyson, Uncertainty estimates for theoretical atomic and molecular data, J. Phys. D Appl. Phys. 49 (2016), 363002.
[145] ISO/IEC Guide 98-3:2008, Uncertainty of Measurement-Part 3: Guide to the Expression of Uncertainty in Measurement (GUM: 1995).
[146] J. Robertson, Amorphous carbon, Adv. Phys. 35 (1986) 317–374.
[147] J. Robertson, Hard amorphous (diamond-like) carbons, Prog. Solid State Chem. 21 (1991) 199–333.
[148] M.B.P. Nigam, M.K. Sundaresan, T.-Y. Wu, Theory of multiple scattering: second Born approximation and corrections to Molière's work, Phys. Rev. 115 (1959) 491.
[149] I. Adesida, R. Shimizu, T.E. Everhard, A study of electron penetration in solids using a direct Monte Carlo approach, J. Appl. Phys. 51 (1980) 5962.
[150] L. Zommer, A. Jablonski, G. Gergely, S. Gurban, Monte Carlo backscattering yield (BY) calculations applying continuous slowing down approximation (CSDA) and experimental data, Vacuum 82 (2008) 201–204.